# 5
# Design and Development of High-Temperature Absorber Reflector ($ZrO_x$/ZrC-ZrN/Zr) Tandem Spectrally Selective Coatings

## 5.1 INTRODUCTION

Numerous oxide and nitride based solar selective coatings are investigated for high-temperature applications. A historical development of high-temperature SSCs is discussed in section 2.4.3. Among them, titanium, zirconium, or hafnium metal carbides, oxides, and nitrides exhibit a higher degree of spectral selectivity, showing promise for spectrally selective coatings, especially for high temperature applications. These carbides and nitrides absorber-reflector tandem structures such as $TiN_x$, $ZrN_x$, and $ZrC_xN_y$ with silver (Ag) as an infrared reflector on different substrates have been investigated as the solar selective coatings for desired solar absorptance and thermal emittance properties [Kennedy, 2002]. These selective absorbers exhibit stability problems at high temperature ~ 350 °C (even in a vacuum) due to the agglomeration issues of the silver metal reflector. However, these structures showed good solar thermal performance at room temperature [Ihara *et al*, 1977]. Poor thermal stability of this metal reflecting layer at high temperature (~ 350°C) degrades the infrared reflecting properties, causing an enhancement in the emissivity for SSCs. Sputtered $ZrC_xN_y$ selective absorber surfaces on aluminum-coated oxidized stainless-steel are thermally stable up to 600°C (likely in a vacuum but not specified in reported work) [Ihara *et al*, 1977]. Lazarov et. al., has replaced Ag with Zr as an infrared reflector layer in sputtered $ZrO_x/ZrC_x/Zr$ absorber-reflector tandem solar selective structures and observed high optical selectivity with $\alpha/\varepsilon$(20°C) =0. 90/0.05 and thermal stability on stainless-steel and quartz substrates up to 600°C and 800°C in vacuum, respectively [Lazarov and Mayer, 1997, 1998]. There are still several challenges associated with such high temperature solar selective coatings, especially for their long term thermal stability, cyclability, and environmental stability (corrosion etc.). Keeping in mind these constraints, continuous efforts are in progress towards the development of such coatings, which may provide enhanced spectral selectivity and thermal stability to realize the better power generation efficiencies.

In this study, attempts are made to design and develop a high temperature absorber-reflector ($ZrO_x$/ZrC-ZrN/Zr) tandem structure based spectrally selective coatings. This includes: (i) the optimization of zirconium film as a metal reflector with minimum emittance, (ii) the optimization of zirconium carbide-nitride absorber layer with enhanced solar performance and temperature stability, and (iii) understanding microscopic origin of absorptance, emittance and other physical properties in such system. The developed $ZrO_x$/ZrC-ZrN/Zr structures on copper and stainless substrates were further subjected to numerous characterizations to understand (i) the impact of growth conditions on mechanical properties, and (ii) the impact of corrosion and thermal treatment on physical properties and their correlation with the solar thermal performance.

## 5.2 DESIGN OF $ZrO_x$/ZrC-ZrN/Zr ABSORBER-REFLECTOR TANDEM STRUCTURES FOR SPECTRALLY SELECTIVE COATINGS

The schematic of $ZrO_x$/ZrC-ZrN/Zr absorber-reflector tandem structure is shown in Figure 5.1(a), for different substrates such as stainless steel (SS), copper (Cu), aluminum (Al) and glass. Here, a metallic Zr layer is used to achieve infrared reflection in the desired wavelength range on these substrates against the conventional infrared reflecting layers such as silver and aluminum, where stability is limited up to ~ 350°C, even in a vacuum [Ihara *et al.*, 1977]. Against these conventional infrared reflectors, Zr metal reflector provides high infrared reflectivity with enhanced thermal stability against high temperature because of its refractory nature [Zhang *et al.*, 2003]. In conjunction with the infrared reflector layer, the absorber layer is also critical and needs to be optimized for the maximum absorption of incident solar radiation. ZrC-ZrN absorber layers are investigated and optimized by controlling the free electron density in the d-band of Zr transition metal and nitride fraction in carbide matrix. This can be achieved by manipulating the stoichiometry and nitrogen concentration in ZrC-ZrN absorber layers. The enhanced electron density in ZrC-ZrN spectrally selective absorber layers will introduce plasmonic absorption in the long wavelength region of the solar spectrum. In conjunction with intrinsic absorption, this additional plasmonic absorption, in ZrC-ZrN absorber layers, will enhance the total absorption of the incident solar radiation over an extended wavelength range [Seraphin, 1979; Kittel, 1995]. We utilized this concept to optimize the optical properties of ZrC-ZrN absorber layers to achieve the maximum spectral selectivity and thus, the enhanced solar absorption, by varying nitrogen concentration. Antireflection structures are used to minimize the back reflection into the ambient and any microstructural damages to the absorber layer directly. In this work, $ZrO_x$ antireflecting layer was fabricated on ZrC-ZrN absorber layer, as explained in Figure 5.1. $ZrO_x$ antireflection layer not only reduces the back reflection but also enhances the thermal and environmental resistivity of fabricated spectrally selective structures. We observed that $ZrO_x$/ZrC-ZrN/Zr absorber–reflector tandem layered structures exhibit absorptance are 0.81-0.88, 0.81 - 0.90, 0.82 - 0.90 and 0.86 - 0.89 and emittance ~ 0.04, ~ 0.1, ~ 0.05 and ~ 0.05 on SS, Cu, Al and glass substrates, respectively. The detailed fabrication process and intensive characterization of these designed spectrally selective coatings are discussed in the following sections.

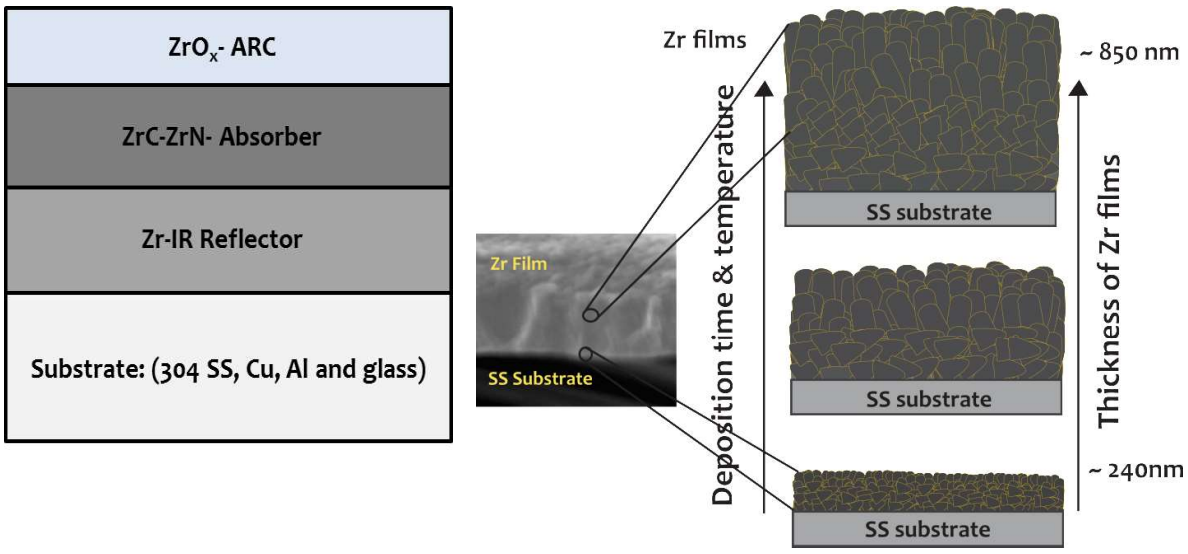


**Figure 5.1 :** (a) Schematic representation of $ZrO_x$/ZrC-ZrN/Zr absorber-reflector tandem structures on stainless steel (SS), copper (Cu), aluminum (Al) and glass substrates. (b) Growth schematic of Zr metallic film on SS substrate with varying deposition time and temperature.

## 5.3 OPTIMIZATION OF SPUTTERED ZIRCONIUM FILM AS AN INFRARED REFLECTOR

The optimization of zirconium (Zr) layer is important to achieve the desired solar thermal performance. This includes the process parameters and effective thickness, which may provide the minimum thermal emittance. Zirconium thin films were deposited using DC sputtering at a working pressure ~ 2.5 x $10^{-2}$ mbar. The argon (Ar) sputtering gas was introduced at a flow rate of 50 SCCM (standard cubic centimeter per minute at STP) into the chamber to the mentioned working pressure for deposition. The process parameters such as time and temperature of deposition have been optimized keeping the power constant. The synthesis processes including the cleaning of substrates are discussed in detail by Usmani et al. [Usmani *et al.*, 2016].

### 5.3.1 Results and Discussion

#### *5.3.1.1 Structural Analysis*

X-ray diffraction measurements are shown in Figure 5.2 for Zr/SS structures, deposited for different time intervals and substrate temperatures. X-ray diffraction data (Fig. 5.2), suggests that the sputtered deposited Zr films are polycrystalline in nature, showing a mixture of cubic and hexagonal zirconium phases. The deposition time has strong effect on the crystallographic phase, as can be seen from the X-ray diffraction patterns (Fig.5.2a (i, ii, iii, iv, v & vi)). For 30 min deposition time (low thickness), Zr thin film is nearly amorphous, and only chromium peaks at $2\theta = 43.54^{o}$, $44.44^{o}$ and $50.55^{o}$, from SS substrate (ICDD PDF#: 01-088-2323), can be seen. A very less intense peak at $2\theta = 29.89^{o}$ has been observed, which may correspond to of zirconium oxide (111) diffraction plane (ICDD PDF#: 049-1642). The onset of this oxide phase is attributed to the presence of residual oxygen in the deposition chamber. However, for 60 min deposition, Zr film showed a diffraction peak at $2\theta = 31.97^{o}$ correspond to (100) plane for hexagonal zirconium crystallographic phase (ICDD PDF#: 03-065-3366), in conjunction with substrate diffraction peaks. As the deposition time of Zr film was increased, Zr film exhibited (111) preferred cubic crystallographic phase at $2\theta = 34.386^{o}$ (ICDD PDF#: 01-088-2329). The phase development of Zr films on glass substrate also followed the same pattern as on SS substrates with varying deposition time. The substrate temperature may also play an important role in the crystalline quality of sputtered films and has been used an optimization parameter for Zr thin films in the present study [Bilgin *et al.*, 2005]. Figure 5.2b shows the X-ray diffraction pattern of Zr films deposited on SS substrate at different temperatures, keeping the deposition time constant for 2 hours. The films deposited at different temperature are polycrystalline and polyphase in nature with simultaneous cubic and hexagonal zirconium crystallographic phases. At low substrate temperature, the film exhibited (111) preferred orientation of cubic zirconium phase of at $2\theta = 34.386^{o}$ (ICDD PDF#: 01-088-2329). However, (100) orientation of hexagonal zirconium film is favored with increasing temperature from $350^{o}$C to $500^{o}$C. The oxide impurity starts reducing with increasing both deposition time and temperature, as shown in Figure 5.2, where the observed zirconium oxide diffraction peak has reduced for films deposited at higher temperatures and for longer durations.

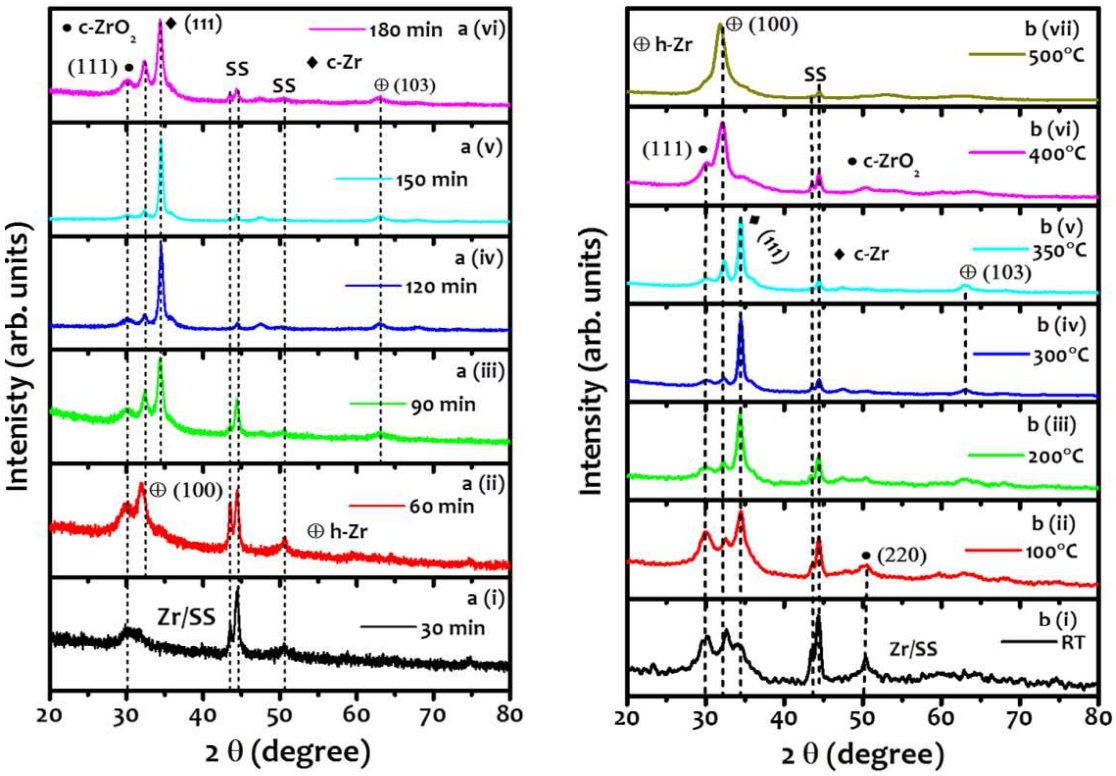


**Figure 5.2 :** X-ray diffraction spectra of the Zr films sputtered at different **(a)** deposition time and **(b)** deposition temperature on stainless steel substrates.

The full width half maxima (FWHM), B, grain size (t) [Cullity, 1972], dislocation density (δ)[Williamson and Smallman, 1956], and strain (ε) [Velumani, *et al.,* 2003] of the films were calculated for the preferential orientations and results are summarized in Tables 5.1 & 5.2 for the Zr films deposited on SS substrate with varying deposition time and substrate temperature. However, details of these parameters on glass substrates are described elsewhere [Usmani *et al*, 2016c]. The crystalline size increases and the dislocation density decreases with increasing the deposition time and substrate temperature, initially and thereafter a slight decrease in grain size and increase of strain and dislocation density are noticed. Moreover, the average grain size increases with increasing deposition time (i.e. with increasing the thickness), but for higher deposition times (i.e. higher thicknesses) the decrease in grain size may be due to the formation of additional smaller grains on the larger grains, as also observed by Velumani et al. [Velumani *et al.,* 2003].

The similar trends have been observed for grain size, dislocation density, and strain with increasing the substrate temperature and measured values are summarized in Table 5.2. The dislocation density and strain are the demonstration of dislocation network in the films. The decrease in the strain and dislocation density suggests the formation of better quality films at higher substrate temperatures. Moreover, smaller *B* (HWFM) values and larger *t* denotes better crystallization of the films. The minimum emittance values were obtained from Zr films with larger grain size, lower dislocation density, and lower strain values. The schematic of zirconium thin film growth on stainless steel substrate has been illustrated in Figure 5.1(b), as a function of deposition time and thickness. Zirconium film showed highly disorder phase at the lower thickness, up to ~ 240 nm, which is formed due to large mismatch between the lattice parameters of Zr and SS or glass substrate. As thickness increases with time, probably the initial Zr layer may act as a buffer layer for upper Zr thin film structure, and thus, resulting in enhanced crystallinity and reduced defect density, as observed in XRD measurements and

summarized in Table 5.1 & 5.2. Finally, the pure crystallographic phase has been deposited due to the pseudo lattice matching of Zr metallic thin film structures, which has shown the lowest emittance values, as explained later.

**Table 5.1 :** Microstructural properties of Zr films with varying deposition time on SS substrates

| *Time (min)* | *B* (rad) | t (nm) | $\delta \times 10^{16}$ (line/m$^2$) | $\varepsilon$ |
|---|---|---|---|---|
| 90 | 0.711 | 11.7 | 0.7305 | 2.2527 |
| 120 | 0.586 | 14.2 | 0.4959 | 1.856 |
| 150 | 0.516 | 16.12 | 0.3848 | 1.6348 |
| 180 | 0.692 | 12.01 | 0.6932 | 2.1924 |

**Table 5.2 :** Microstructural properties of Zr films with varying deposition temperature on SS substrates

| *T* (°C) | *B* (rad) | t (nm) | $\delta \times 10^{16}$ (line/m$^2$) | $\varepsilon$ |
|---|---|---|---|---|
| 100 | 0.966 | 8.61 | 1.3489 | 3.06 |
| 200 | 0.785 | 10.6 | 0.8899 | 2.4871 |
| 300 | 0.583 | 14.27 | 0.4959 | 1.8471 |
| 350 | 0.638 | 13.04 | 0.588 | 2.021 |

#### *5.3.1.2 Microstructural Analysis*

Three-dimensional (3D) AFM surface morphology of Zr films, deposited on SS substrate, at a different substrate temperature (from room temperature (RT) to 500 °C) are shown in Fig. 5.3(a, b, c, d, e, f & g). Films show denser granular morphology, with enhanced granular sizes with increasing the substrate temperature. These results also correlate with the observed X-ray diffraction measurements, as explained in the previous section. Root mean square (RMS) surface roughness ($R_q$), average surface roughness ($R_a$) and grain size were calculated from the scanned surface morphology. RMS surface roughness and grain size are shown in Figure 5.4 (a & b) as a function of deposition time and substrate temperature on SS substrate. The RMS surface roughness increases (Figure 5.4a) with increasing the deposition time. However, after a certain deposition time, RMS surface roughness starts decreasing, suggesting that the defects are reduced relatively for thicker films. Moreover, at higher deposition time (180 min), RMS surface roughness starts increasing, suggesting the onset of the surface defects because of local agglomeration or other related synthesis defects. The RMS surface roughness is almost same up to 300°C with deposition temperature, however, start decreasing after 300°C (Figure 5.4b). The grain size of the film increases with temperature up to 200°C initially and remains nearly unaffected from 200°C to 400°C deposition temperature. This starts increasing again at higher temperatures, which is also consistent with the X-ray diffraction patterns, where FWHM of the observed diffraction has decreased with increasing temperature. RMS surface roughness and grain size of zirconium films deposited on glass substrate show similar characteristics [Usmani *et al*, 2016c]. SEM micrographs of Zr films deposited on SS substrate with varying substrate

temperature are shown in Figure 5.3(a, b, c, d, e, f & g). The surface micrographs showed dense granular microstructure with the substrate imprints. The growth and development of surface morphology are similar to that of AFM measurements. The low surface roughness of the film coatings is important to obtain low thermal emittance, as emittance relies on the surface properties, especially the smoothness of the surface structure [Duffie and Beckman, 1980].

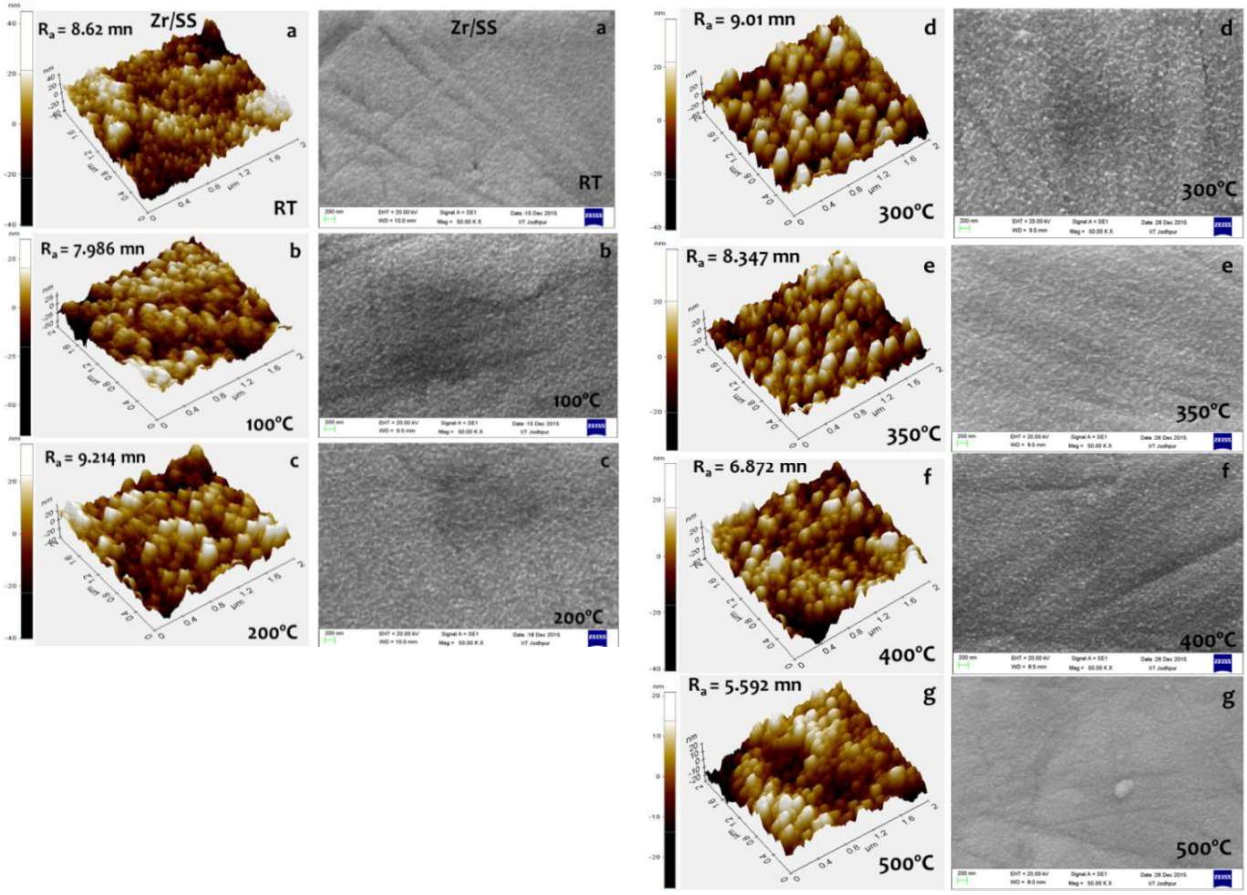


**Figure 5.3 :** AFM surface morphology and SEM micrographs images of sputtered deposited Zr thin films on Stainless steel substrate having substrate temperature: **(a)** RT, (b) 100°C, **(c)** 200°C, **(d)** 300°C, **(e)** 350°C, **(f)** 400°C, **(g)** 500°C.

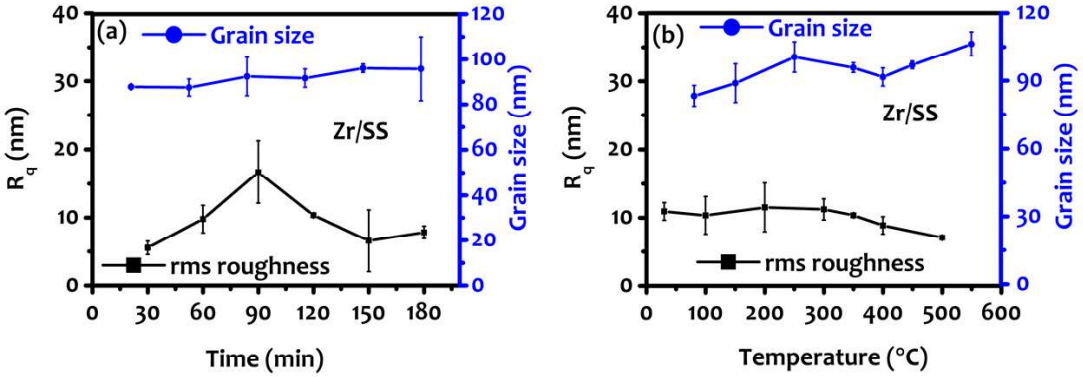


**Figure 5.4 :** Root mean square (RMS) surface roughness and grain size of Zr films deposited on SS substrate at different (a) deposition time and (b) substrate temperature.

The thickness of these films was measured using AFM across the step between Zr film and substrate, as explained in Figure 5.5(a) inset, and variation in thickness versus deposition time & temperature are plotted in Figures 5.5(a) & 5.5(b) respectively. These measurements suggest that film thickness increases continuously, however, it saturates at or above 300 $^{o}$C, as shown in Figure 5.4(b).

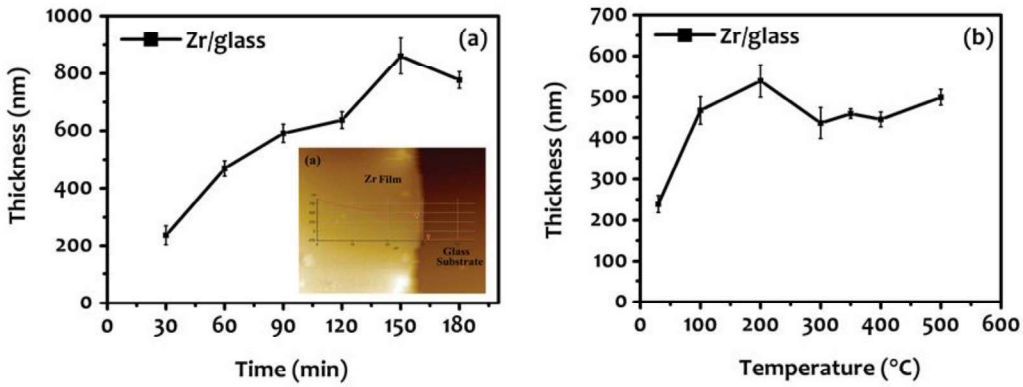


**Figure 5.5 :** Film thickness of Zr film on a glass substrate deposited with varying **(a)** deposition time and **(b)** substrate temperature.

### *5.3.1.3 Optical Analysis*

The reflectance spectra of Zr films are shown in Figure 5.6(a & b), in 2.5 – 25 μm wavelength range. The calculated emittance values are summarized in the inset of the respective graphs (Fig.6a), suggesting that the emittance values decrease with increasing deposition time and thus with the thickness. The minimum emittance value is ~ 0.12, observed for 120 min or larger deposition time. The calculated emittance values of Zr films deposited with varying temperature on SS substrate are shown in the inset of Figure 6(b). The emittance value has decreased from 0.44 to 0.14 with increasing the substrate temperature. The minimum emittance values on SS substrate are observed at 350$^{o}$C deposition temperature. Thus, the optimal conditions of Zr reflector layer depositions, such as substrate deposition temperature, 350°C and deposition time, 2 hour, have been used for depositing the Zr metal reflector in tandem ZrOx/ZrC-ZrN/Zr selective structure on different substrates.

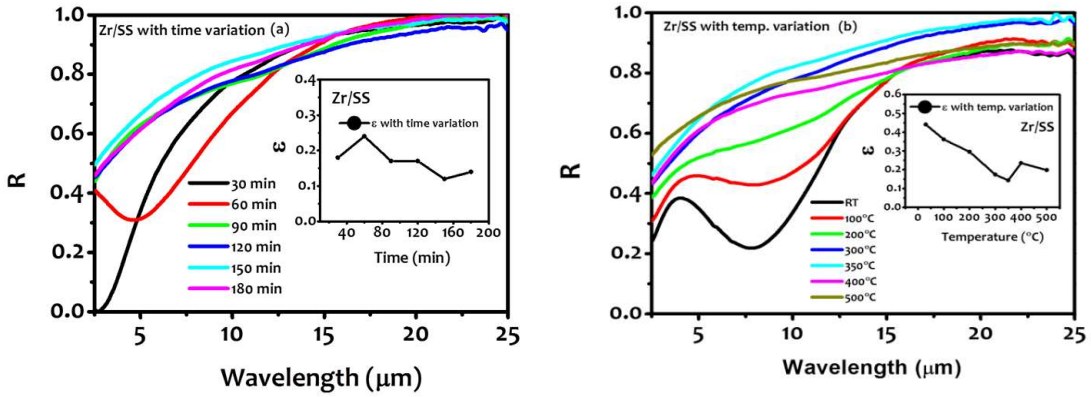


**Figure 5.6 :** Reflectance spectra of the Zr film deposited on SS substrate **(a)** with changing time from 30 min to 180 min: in inset show the calculated emittance vs. deposition time. **(b)** With changing substrate temperature from room temperature to 500°C: in inset show the calculated emittance values vs. substrate temperature.

## 5.4 OPTIMIZATION OF $ZrO_X$/ZrC-ZrN/Zr ABSORBER-REFLECTOR TANDEM STRUCTURES

Optimized zirconium metal infrared reflector (IR) was used in zirconium carbonitride based absorber-reflector tandem structure ($ZrO_x$/ZrC-ZrN/Zr) as infrared metal reflector layer. In this section, the details for optimized zirconium carbide-nitride absorber layer on SS, and Cu substrates are discussed. The optimized process has also been investigated for Al and glass substrates and similar results have been observed and discussed in details by Usmani et al. [Usmani, *et al.*, 2016a]. Spectrally selective tandem absorber-reflector $ZrO_x$/ZrC-ZrN/Zr structures were prepared on different substrates using DC/RF magnetron sputtering system. The samples are labeled as S1 to S6 with increasing nitrogen flow rate used during the synthesis of ZrC-ZrN absorber layers. Details of substrates cleaning, deposition process, and characterization techniques such structural, microstructural, surface, elemental, vibrational, optical properties and thermal stability are explained in detail by Usmani et al. [Usmani *et al.*, 2016b].

### 5.4.1 Results and Discussion

#### *5.4.1.1 Structural Analysis (X-ray Diffraction and Raman Spectroscopy)*

The detailed X-ray diffraction analysis of $ZrO_x$/ZrC-ZrN/Zr solar selective coatings in sequential deposition order, including substrates are described in Usmani et al. published work [Usmani *et al.*, 2016b]. We also collected X-ray diffraction spectra of the selective absorber, which is prepared at different nitrogen flow conditions, on both SS and Cu substrates. The representative XRD spectra of solar selective structures on SS substrates are plotted in Figure 5.7(a)(i, ii, iii, iv, v & vi) for different nitrogen flow rates used for fabrication of ZrC-ZrN absorber layers. We noticed similar phases for Zr infrared reflector layers, a ZrC-ZrN absorber layer, and $ZrO_x$ antireflection layers in all these samples with different nitrogen flow rates. X-ray diffraction spectra on Cu substrates are also identical to that on SS substrates. To understand the effect of nitrogen flow rates in ZrN phase evolution, we calculated the relative phase fraction of ZrN in ZrC matrix. The ZrN phase fraction was increasing with an initial increase in nitrogen flow and exhibited maxima at 12.5 SCCM, followed by a decrease with any further increase, as explained in Figure 5.7(b) for layered structures on substrates, stainless steel, and copper.

Room temperature micro-Raman spectroscopic measurements were carried out for absorber-reflector tandem ($ZrO_x$/ZrC-ZrN/Zr/Substrate) structure selective coatings and are shown in Figure 5.8. The left panel represents Raman spectra in the range of 200 $cm^{-1}$ – 2000 $cm^{-1}$, for ZrC-ZrN/Zr absorber layer, and sequential antireflecting $ZrO_x$/ZrC-ZrN/Zr layered structures for sample S5 on both the substrates, Figure 5.8(a & b(i)) and Figure 5.8(a & b(ii)). The observation of characteristic ZrN vibrational modes in ZrC-ZrN absorber layer substantiates the presence of dominating ZrN phase, as observed from XRD measurements also; even for absorber layer with the lowest nitrogen flow rate. The low energy modes ~ 290 $cm^{-1}$ and 360 $cm^{-1}$ represent the characteristic modes for the rock salt ZrN structure, consistent with the reported literature [Han *et al.*, 2005]. The higher wave number ~1350 and 1580 $cm^{-1}$ vibrational modes show the contribution from C-C and C-N bonding. These numbers are very close to the C-C bonds in intrinsic carbon systems and are found in disordered graphite systems [Kurt *et al.*, 2000; Chowdhury *et al.*, 1999]. The close resemblance in C-C and C-N vibrational frequencies make it difficult to identify the contribution of these vibrational modes in ZrC and ZrN systems independently. Raman spectra for all $ZrO_x$/ZrC-ZrN/Zr/SS samples from S1 to S6, with different nitrogen flow rates are plotted in Figure 5.8(right panel). The results are similar with the observed microscopic changes as explained in previous sections.

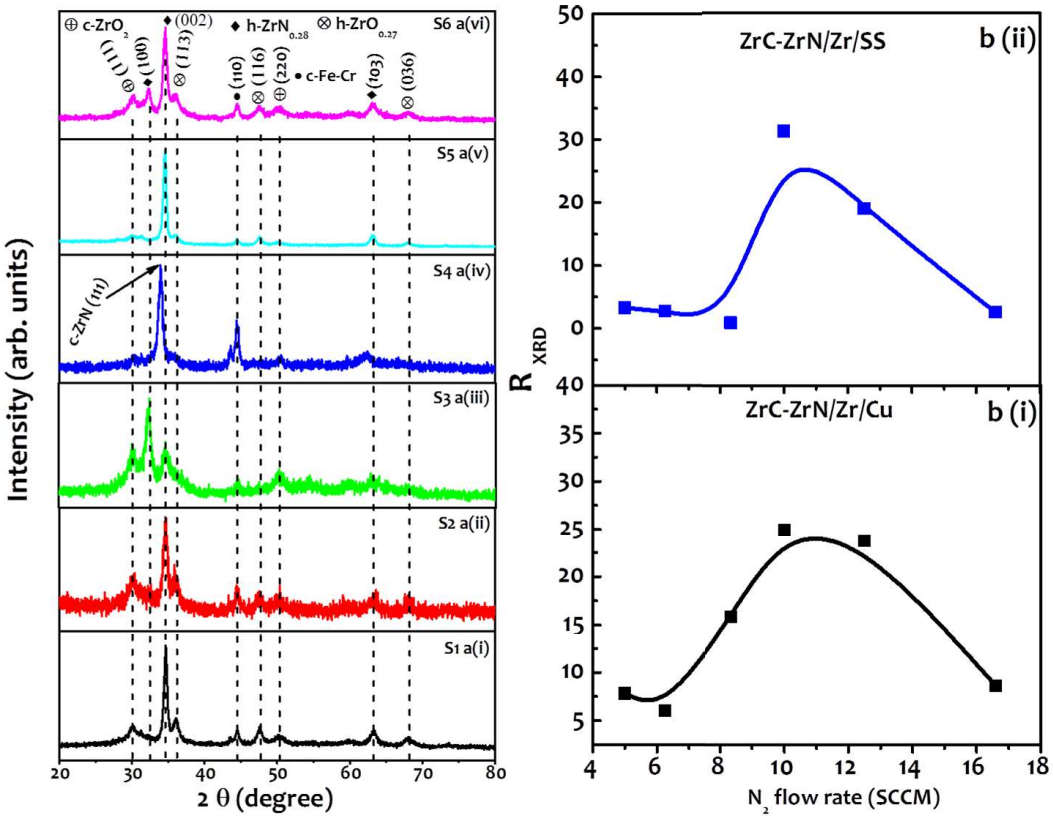


**Figure 5.7 :** X-ray diffraction spectra of $ZrO_x$/ZrC-ZrN/Zr absorber-reflector tandem structures deposited on SS substrate for all samples prepared under different gas flow conditions **a(i)** 5sccm S1; **a(ii)** 6.25sccm S2; **a(iii)** 8.34sccm S3; **a(iv)** 10.0sccm S4; **a(v)** 12.5sccm S5 and **a(vi)** 16.6sccm S6; and (b) nitride to carbide phase fraction with varying nitrogen flow rates in (i) ZrC-ZrN/Zr/Cu and (ii) ZrC-ZrN/Zr/SS absorbers layers.

The $ZrO_x$ antireflecting layer was deposited on the ZrC-ZrN/Zr layer coated substrates. The Raman spectrographs of $ZrO_x$/ZrC-ZrN/Zr multilayer structure for sample S5 are plotted in Fig. 5.8 a(ii) and 5.8 b(ii) for SS and Cu substrates, respectively. The observed mode at ~ 610 $cm^{-1}$ is the characteristic mode of the tetragonal $ZrO_x$ system. This is also a characteristic mode for monoclinic $ZrO_x$ system [Siu *et al.*, 1999; Sharma *et al.*, 2014; Keramidas and White, 1974]. The presence of this characteristic $ZrO_x$ mode suggests the possibility for the admixture of tetragonal and monoclinic phase in room temperature grown $ZrO_x$ antireflection layers. The presence of such multiphase is possible for low-temperature grown $ZrO_x$ thin films. This mode is absent in ZrC-ZrN absorber layer, suggesting the oxide free ZrC-ZrN absorber layers. The Raman vibrational mode at ~ 1210 $cm^{-1}$ has been assigned as a second order Raman mode for 610 $cm^{-1}$ modes for the tetragonal $ZrO_x$ system. The penetration depth (~ 1/2 α, where α is absorption coefficient) of incident 532 nm (~ 2.33eV) green laser light used in these experiments is ~ 1μm, much larger than the $ZrO_x$ layer thickness. The large penetration depth of the incident laser light has been observed in terms of strong interaction with the underneath ZrC-ZrN absorber layer, where all Raman modes, observed in case of pristine absorber layers, are also present in conjunction with $ZrO_x$ vibrational modes.

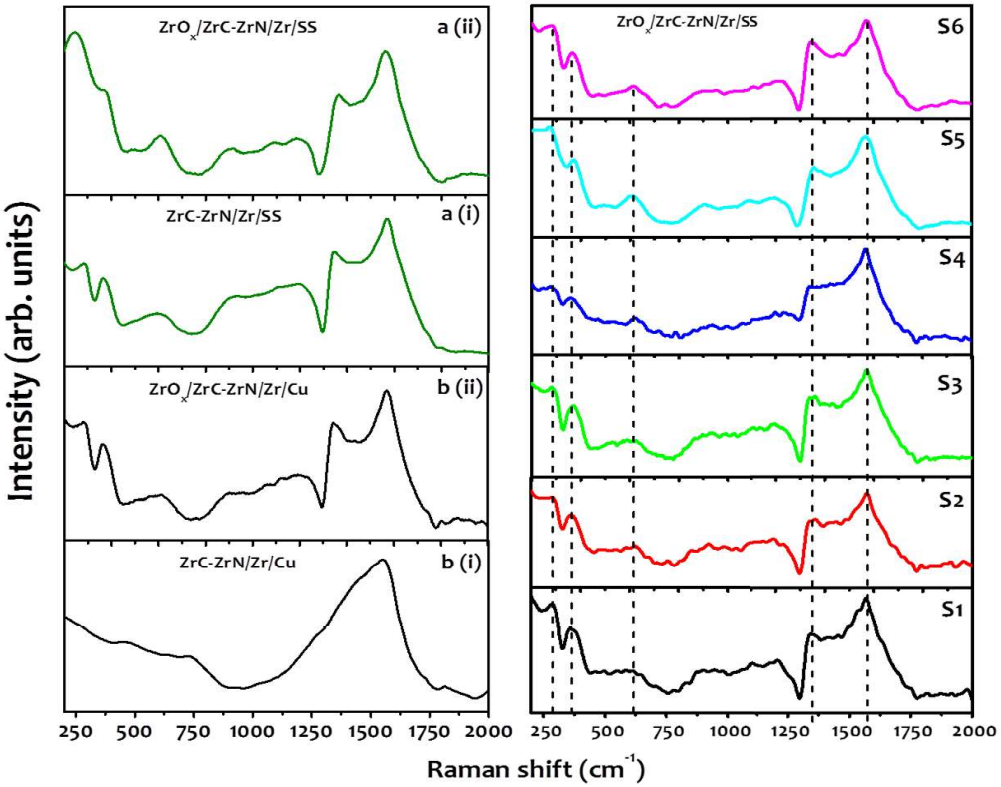


**Figure 5.8 : (Left panel)** Raman spectrographs for ZrC-ZrN/Zr structures on SS a(i) and on Cu substrate b(i) and for $ZrO_x$/ZrC-ZrN/Zr structures on SS a(ii) and on Cu substrate b(ii) for S5 sample; and **(Right panel)** right panel represents Raman spectrographs for all $ZrO_x$/ZrC-ZrN/Zr structures on SS substrates, prepared under different nitrogen flow conditions.

### *5.4.1.2 Microstructure, Surface Roughness and Elemental Analysis*

The microstructure, roughness, and elemental compositions are analyzed using SEM and AFM measurements on these solar selective coatings. The scanning electron micrographs of $ZrO_x$ top surfaces for sample S5 on both SS and Cu substrates are shown in Figure 5.9(a & b)(right panel). We observed that developed surfaces are smooth with some substrate surface imprints, developed with the deposition of thin films. These surface imprints are not desired and may degrade the solar thermal response, especially the emissivity of fabricated tandem absorber-reflector structures. In addition, to such surface imprints, developed surfaces show micro-structured columnar grains, as observed in AFM micrographs, and explained in the three-dimensional AFM micrographs, Fig. 5.9 a(iii)(left panel) for sample S5 on SS substrate. In addition to the top $ZrO_x$ surfaces, we also collected three-dimensional images of individual, Zr infrared reflector and ZrC-ZrN absorber layers after sequential fabrication, to understand the evolution of microstructures in these solar selective coatings and detailed atomic force micrographs are shown in Figure 5.9 (left panel). The surface roughness of Zr metal layer is maximum ~ 23.5 nm with hillock like morphological patterns. This starts reducing with sequential layer deposition and observed surface root mean square (RMS) roughnesses are ~ 11.21 nm and 13.75 nm with island type morphological structures for ZrC-ZrN absorber and $ZrO_x$ antireflecting layers, respectively. The similar observations have also been observed for $ZrO_x$/ZrC-ZrN/Zr/Cu spectrally selective coatings structures and details are present in Usmani et al., published work [Usmani *et al.*, 2016b].

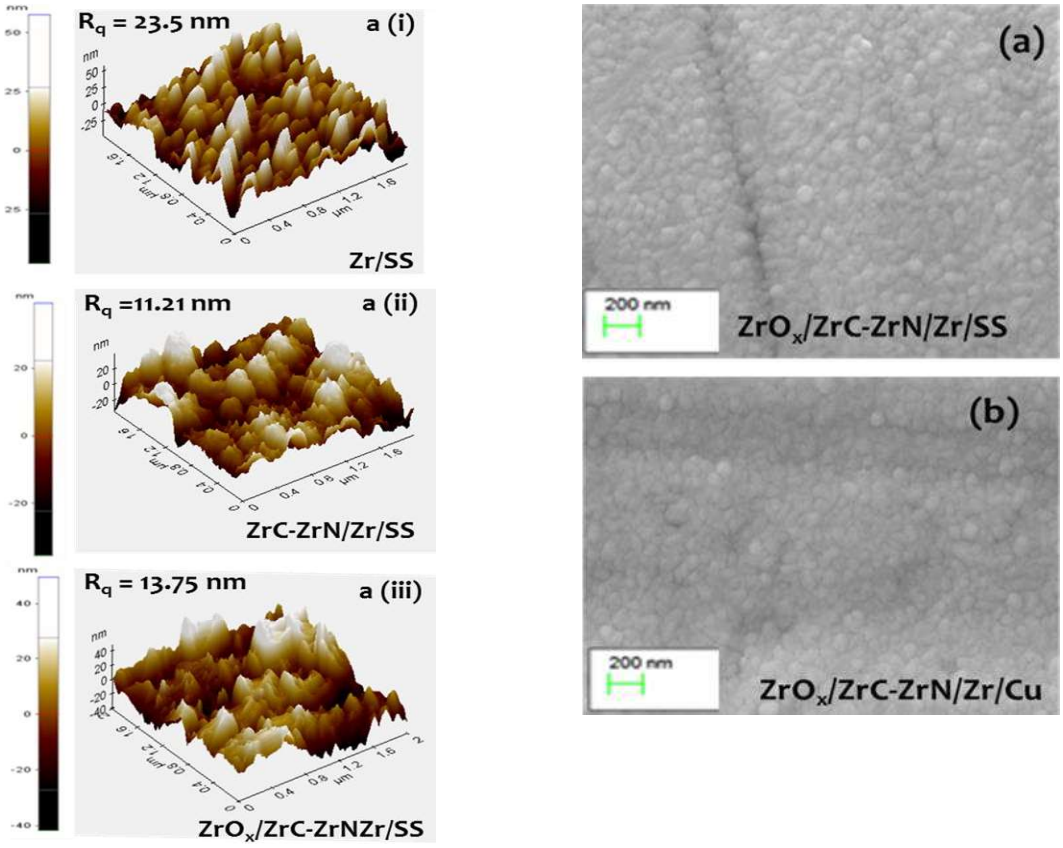


**Figure 5.9 : (Left panel)** Three-dimensional AFM images of Zr layers on SS a(i) substrate; ZrC-ZrN layer deposited on Zr coated SS a(ii) substrate, and $ZrO_x$/ZrC-ZrN/Zr coating deposited on SS a(iii) substrate for S5 sample. **(Right Panel)** SEM micrographs of the top surface of $ZrO_x$/ZrC-ZrN/Zr absorber-reflector tandem structure on (a) SS (b) Cu substrate.

The elemental analysis has been carried out using EDX measurements for Zr, C, and N atomic fractions in these fabricated ZrC-ZrN absorber layers as a function of $N_2$ flow rate. The results are summarized in Table 5.3 for SS and Cu substrates. We observed the respective variation in Zr, C, and N atomic fractions by varying $N_2$ flow during the synthesis of these tandem absorber-reflector structures. We found that Zr atomic fraction is slowly increasing and showed the maximum Zr atomic fraction for sample S5 at 12.5 SCCM $N_2$ flow rate. The additional increase in $N_2$ flow rate has resulted in the reduction of Zr atomic fraction. However, we noticed that N atomic concentration is ~ 36%, much larger with respect to that of carbon ~ 27% in the case of S5 sample. Moreover, nitrogen atomic fraction initially increases with increasing flow rate and start decreasing at a higher flow rate, which correlates with X-ray diffraction analysis of ZrN fraction in ZrC matrix (Figure 5.7b).

**Table 5.3 :** Measured elemental atomic fractions in ZrC-ZrC absorber layers for different samples with respective nitrogen flow conditions used for synthesis of this structure

| S.No. | $N_2$ (SCCM) | ZrC-ZrN/Zr/SS | | | ZrC-ZrN/Zr/Cu | | |
|---|---|---|---|---|---|---|---|
| | | Zr (atm. %) | C (atm. %) | N (atm. %) | Zr (atm. %) | C (atm. %) | N (atm. %) |
| S1 | 5.0 | 26.93 | 36.42 | 36.65 | 21.97 | 37.12 | 40.91 |
| S2 | 6.25 | 25.56 | 32.53 | 41.91 | 24.97 | 33.02 | 42.01 |
| S3 | 8.34 | 28.67 | 27.33 | 44.0 | 28.76 | 25.54 | 45.70 |
| S4 | 10.0 | 35.18 | 24.09 | 40.37 | 30.70 | 30.13 | 39.17 |
| S5 | 12.5 | 35.98 | 27.67 | 36.36 | 34.14 | 28.25 | 37.61 |
| S6 | 16.66 | 32.25 | 27.01 | 40.65 | 30.02 | 29.89 | 40.09 |

#### *5.4.1.3 Optical Properties*

The reflectance versus wavelength measurements are summarized in Figure 5.10 (a & b) for $ZrO_x$/ZrC-ZrN/Zr structures in ~ 0.3 μm – 25 μm wavelength range on SS and Cu substrates respectively. These are used to calculate the absorptance and emissivity, using equations (2.5) and (2.7) respectively. The calculated solar absorptance varies ~ 0.81 to 0.88 and emissivity ~ 0.04 to 0.2 with the nitrogen flow, and results are plotted in Figure 5.10(c) and 5.10(d) for SS and Cu substrates, respectively. In the case of SS substrates, we found that the absorptance is nearly constant ~ 0.88 up to 8.34 SCCM nitrogen flow rates during deposition, followed by a reduction in absorptance from 0.88 to 0.81 with increasing nitrogen flow rates up to 12.5 SCCM. A similar behavior was also observed for emissivity and results are summarized in Figure 5.10(c). The variation in emissivity of these samples is a bit random in the case of structures fabricated on Cu substrates with respect to that of on SS substrates. This may be due to the surface defects and defects in layered structures, which strongly affect the emissivity of the fabricated structure. This is in accordance with the observed high defect density in the case of Cu substrate with the respect that on SS substrates, as also observed from Raman vibrational investigations and other microstructural studies, explained previously.

The Kubelka-Munk model was used to calculate the absorptance using, $\alpha = \frac{(1-R)^2}{2R}$, where α is absorption coefficient and *R* is reflectance at a wavelength λ [Kubelka, 1931]. The measured normalized absorptance for S5 samples on SS and Cu substrates are plotted in Figure 5.11(a) and 5.11(b) over the entire solar spectrum 0.3-2.5 μm range. Interestingly, we observe three

main absorption regions: (i) low wavelength ~ 0.3- 0.4 μm region, due to density of free electrons in the d-band of transition metal [Seraphin, 1979], (ii) intermediate wavelength ~ 0.4-0.8 μm, due to electronic band gap absorption of the absorbing layer and (iii) long wavelength ~0.8-2.4 μm, due to the excess conduction band electrons in absorbing layer, causing plasmonic absorption. This plasmonic absorption window can be tailored using the nitrogen variation during the synthesis of these solar absorber structures and can be monitored by measuring the electron concentration in these layers.

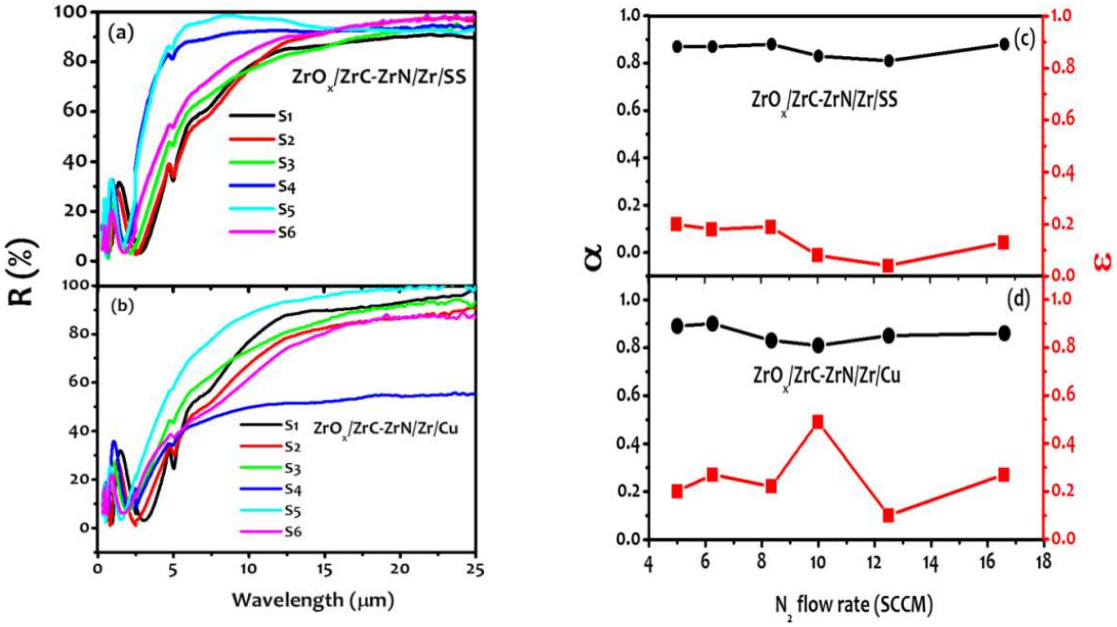


**Figure 5.10 :** % Reflectance of $ZrO_x$/ZrC-ZrN/Zr absorber-reflector tandem structures versus wavelength for different samples on SS **(a)** and Cu **(b)** substrates; calculated absorptance (α) and emittance (ε) values of these $ZrO_x$/ZrC-ZrN/Zr absorber-reflector tandem structures versus nitrogen flow rates for SS **(c)** and Cu **(d)** substrates.

The number of electrons contributing to the plasmonic absorptions in these samples was calculated from $\omega_p^2 = \frac{ne^2}{\varepsilon_0 m}$ where $\omega_p$ is plasmon frequency, $\varepsilon_0$ free space permittivity, and n is the electron density [Kittel, 1995]. The measured Plasmon frequencies are plotted in Figure 5.11(c) and (d) for SS and Cu substrates, as a function of nitrogen flow rate, used for fabrication of these layers. We observed an increase in electron density initially with nitrogen flow rate and exhibit maximum electron concentration ~ 4.0 x $10^{20}$ $cm^{-3}$ at ~ 12.5 SCCM nitrogen flow rate during synthesis. Further increase in nitrogen flow rate resulted in the reduction of electron concentration in these solar absorber layers. Thus, an optimal nitrogen flow rate is important to achieve the maximum electron concentration, thus plasmon absorption, for enhanced long wavelength absorption in ZrC-ZrC absorbing layers. We observed that S5 samples on SS and Cu substrates, with the maximum electron concentration, exhibit maximum absorption and lowest emissivity, thus the maximum solar selectivity. These results suggest a novel approach of introducing plasmonic absorption in the absorber layer to tailor the desired absorption in the infrared (IR) wavelength range.

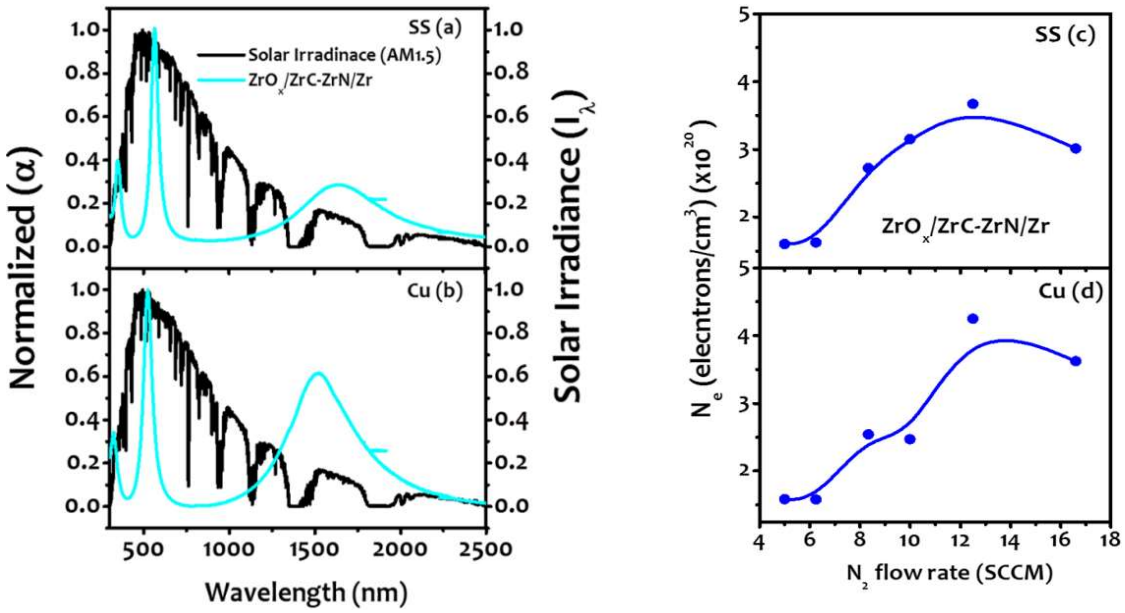


**Figure 5.11 :** Normalized absorptance (α) versus wavelength of $ZrO_x$/ZrC-ZrN/Zr structure on SS (a) and Cu (b) substrates for S5 sample, in conjunction with AM1.5 solar irradiance as a function of wavelength; and estimated electron concentration in ZrC-ZrN absorbing layer versus nitrogen flow rates for absorber structures on SS (c) and Cu (d) substrates.

In conjunction with these absorption mechanisms, interference induced absorption also plays an important role in optimizing the solar absorption in multilayered selective structures. The interference induced absorption relies on refractive index and thickness of the individual layers in the fabricated multilayer structure and substrate properties, whereas intrinsic absorption depends on the extinction coefficient of these layers [Selvakumar *et al.*, 2010; Xinkang *et al.*, 2008]. The normal reflectance measurements are used to calculate the wavelength dependence of refractive index and extinction coefficient using following formulas [Griffiths, 1999].

$$n = \frac{1+R^{1/2}}{1-R^{1/2}} \tag{5.1}$$

$$k = \frac{\alpha\lambda}{4\pi} \tag{5.2}$$

Where n is the refractive index, k is extinction coefficient and R is the reflectance at wavelength λ.

The calculated dispersion curves, i.e. effective refractive index and effective extinction coefficient as a function of wavelengths are plotted for a combination of the sequential layers of the S5 sample in Figure 5.12(a) and 5.12(b)(left panel) on SS substrate. The respective dispersion curves for the Zr metal layer are shown as an inset in Figure 5.12 (a & b) (left panel) in 200 – 800 nm wavelength range and an increase in 'n' and 'k' with the wavelength substantiate the metallic nature and rules out the oxidation of Zr layer. This is important to harness the infrared reflecting properties of the Zr metal layer in multilayer absorber-reflector tandem structures. The measured 'n' and 'k' for ZrC-ZrN/Zr absorber-reflector and $ZrO_x$/ZrC-ZrN/Zr antireflecting coating in conjunction with absorber-reflector structures exhibit sinusoidal variation with wavelength, suggesting the mixed metal-dielectric characteristics of ZrC-ZrN absorber layer. Du et al. have also observed similar observation [Du *et al.*, 2011]. The observed metal-dielectric characteristics are consistent for ZrC-ZrN absorber layer, where ZrC is exhibiting metallic character in ZrN dielectric matrix. In contrast to the sinusoidal nature of

effective refractive index, extinction coefficient exhibits a different behavior and two distinct resonance peaks, responsible for absorption in the layered structure are observed. The low wavelength peak ~ 0.4 – 0.6 μm is due to the optical band absorption from ZrN semiconducting dielectric films and is responsible for absorption in the high energy range of the solar spectrum, whereas as the long wavelength broad peak ~ 1.2 – 1.5 μm is due to the collective oscillations of free electrons (Plasmon absorption) in ZrC-ZrN matrix, mainly coming from ZrC metallic system. These both peaks exhibit redshifts after introducing a $ZrO_x$ antireflecting layer on the ZrC-ZrN absorber layer. The shift in optical band absorption peak is because of the combined effect of ZrN and $ZrO_x$ optical band absorptions, where low energy optical absorption is dominating. In contrast to optical band absorption, a red shift in Plasmon absorption is mainly due to the compensation of free electrons in an absorbing layer with the $ZrO_x$ antireflecting layer. In addition, the relatively large extinction coefficient over the entire solar spectrum for the investigated structure, confirm the enhanced solar absorption and thus, enhanced solar performance. The calculated dispersion curves, i.e. effective refractive index and effective extinction coefficient as a function of wavelengths of S5 samples on Cu substrate show similar behavior and discussed in detail by Usmani et al. [Usmani *et al.*, 2016b].

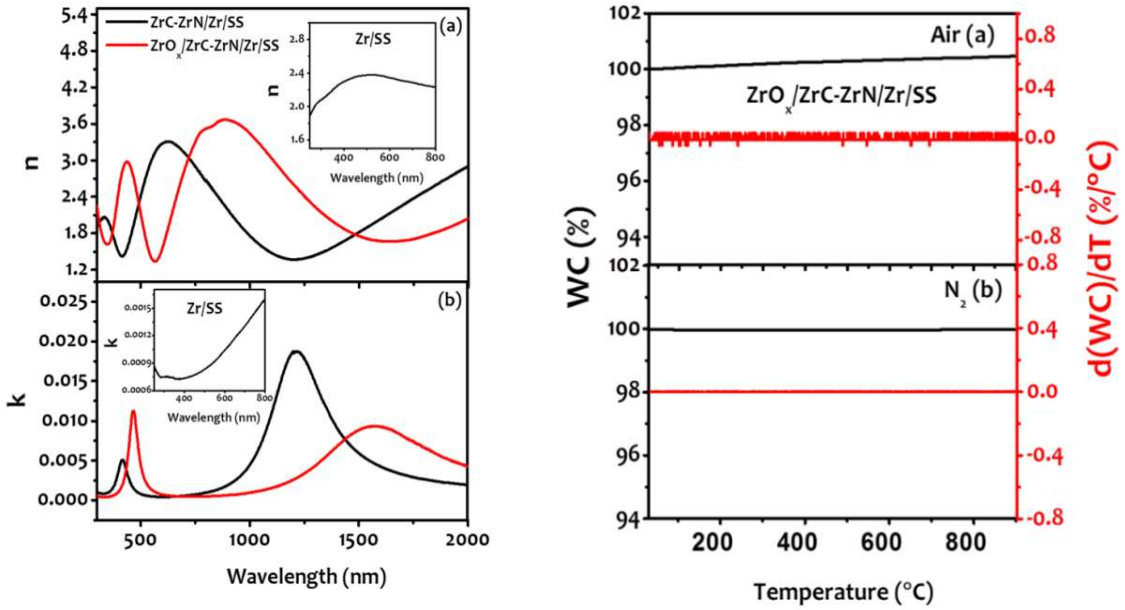


**Figure 5.12 : (Left panel)** Effective refractive index and effective extinction coefficient versus wavelength of sequential layers for $ZrO_x$/ZrC-ZrN/Zr absorber-reflector tandem structures fabricated on SS **(a)** and **(b)** substrate. **(Right panel)** Percentage weight change and first order derivative of weight change as a function of temperature for $ZrO_x$/ZrC-ZrN/Zr absorber-reflector tandem structures on SS **(a)** and **(b)** substrate in air and nitrogen environment.

## 5.5 MECHANICAL PROPERTIES OF $ZrO_x$/ZrC-ZrN/Zr ABSORBER-REFLECTOR TANDEM STRUCTURES

In this section, we will present the detailed studies on mechanical properties, such as Young's modulus and hardness, of the synthesized $ZrO_x$/ZrC-ZrN/Zr absorber-reflector tandem structure on SS and Al substrates. The details about the synthesis of $ZrO_x$/ZrC-ZrN/Zr spectrally selective reflector-absorber tandem structures are explained earlier and the details are also available in Usmani et al. [Usmani *et al.*, 2016b]. Mechanical properties of $ZrO_x$/ZrC-ZrN/Zr structures are investigated using nanoindentation technique. The nanoindenter, used for mechanical measurements, is an integrated accessory with atomic force microscopy system (details are given in section 3.3.9). The Berkovich indenter, a sapphire cantilever with a diamond tip, has been used for indentation on the top surface of $ZrO_x$/ZrC-ZrN/Zr structures. This indenter was initially forced into $ZrO_x$/ZrC-ZrN/Zr surfaces at constant load with the forward (down) speed ~ 0.3μm/s and was kept for 10 s at that depth, followed by unloading at a backward (up) speed ~ 0.3μm/s. Such 10 indentations were made on each sample at different physical locations, to measure the average hardness and Young's modulus using the generated load-displacement curves. AFM was operated in contact mode for all such measurements over 5 x 5 $\mu m^2$ scan areas. The details of calculating the hardness and Young's modulus values are also explained in the section of 3.3.9. In brief, the hardness is obtained as a function of indent depth during loading by dividing the applied load by the projected contact area of the indenter tip. The Poisson's ratio for samples used is ~ 0.3 [Shackelford and Alexander, 2001].

### 5.5.1 Results and Discussion

Nanoindentation method has been used to measure the hardness and Young's modulus of $ZrO_x$/ZrC-ZrN/Zr structures, as the thickness of the entire structure is ~ 600 nm, much larger than the nanoindentation depth ~ 50 nm. This thickness is sufficient to exclude the substrate effect on these measured mechanical properties and thus measured values may represent the values from ZrOx/ZrC-Zr-N/Zr structures only. The measured values of hardness and Young's modulus are summarized in Figure 5.13 for both SS (a) and Al (b) substrates, as a function of nitrogen flow used for the synthesis of ZrC-ZrN absorber layer. The hardness values show strong variation for $ZrO_x$/ZrC-ZrN/Zr structures, with lower nitrogen flow rates used for ZrC-ZrN layer and become nearly constant at 10 or higher SCCM nitrogen flow rates, for both the substrates. The hardness values are prone to the film properties such as films density, microstructure and surface roughness [Chen *et al.*, 2004]. Thus, samples with 10 SCCM or higher nitrogen flow may be showing less surface roughness with optimal density of ZrC-ZrN composite absorber, causing nearly constant hardness values in contrast to lower nitrogen flow rates, where effective density of ZrC-ZrN may be lower and also surface properties may be poor, leading to large variation in hardness values. The maximum selectivity of $ZrO_x$/ZrC-ZrN/Zr tandem structure selective absorber was found around 12.5 SCCM nitrogen flow rate, used for ZrC-ZrN absorber layer as discussed in the above section, suggesting moderate values of hardness may relatively be better for solar thermal performance. Young's modulus also exhibits the similar trend like hardness values, which nearly saturates toward higher nitrogen flow rates, in conjunction with initial large fluctuations.

Hardness and Young's modulus values of $ZrO_2$, ZrN, and ZrC single layer thin film are 13.5 - 19 GPa, 13.4 - 23.5 GPa, 27.6 GPa and 197-210 GPa, 166.4 - 196.3 GPa, 228 GPa, respectively [Chen *et al.*, 2004; Craciun *et al.*, 2010; Zhao *et al.*, 2009]. Interestingly $ZrO_x$/ZrC-ZrN/Zr tandem structures exhibit higher values of hardness as compared to that of $ZrO_2$, ZrN and ZrC single layer thin film hardness values. However, Young's modulus values show contrary behavior with relatively smaller values as compared to $ZrO_2$, ZrN, and ZrC single layer thin film values. This is possible as hardness and Young's modulus in the present work represents the effective values of multilayer tandem structures in contrast to the single layer independently.

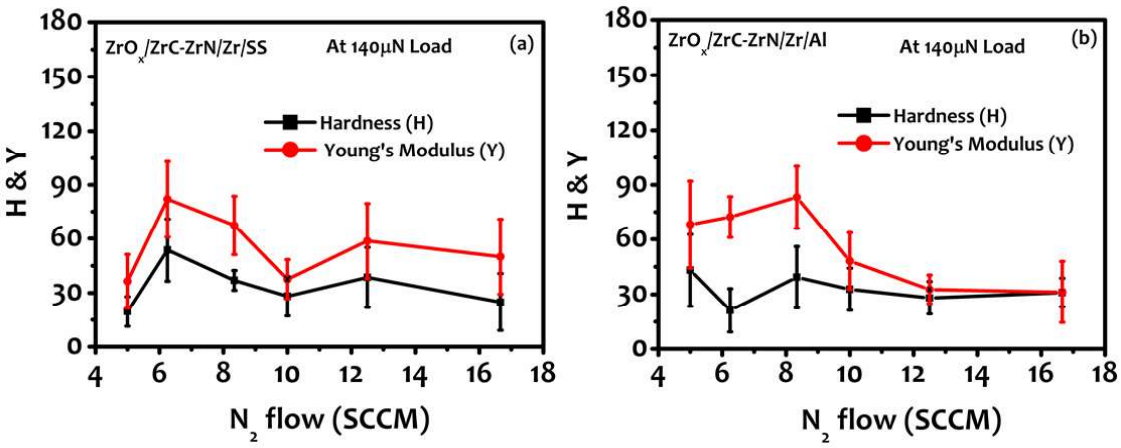


**Figure 5.13 :** (a) Hardness (H) and Young's modulus (Y) of $ZrO_x$/ZrC-ZrN/Zr tandem-absorber film on SS substrate and (b) on Al substrate.

To further understand the details of mechanical properties, as a function of the load as an external variable, we carried out load versus displacement curves at different initial load conditions on the sample with the optimal solar thermal properties $\alpha \sim 0.81$ and $\varepsilon \sim 0.04$, synthesized using 12.5 SCCM nitrogen flow rate. The different load versus displacement curves are shown in Figure 5.14(a) – 5.14(e) and used to measure the hardness and Young's modulus values at these initial load conditions. The respective nanoindentation profiles are shown as an inset in the respective Figures. The profiling of these indentations suggests that depth of such indentations increases with increasing the load with wider marked diameter. The measured H and Y values for this sample as a function of load, within the elastic limit, are summarized in Fig. 5.14(f). These measured values suggest that initially both hardness and Young's modulus values are increasing with load up to ~ 140 μN and reached to nearly constant hardness and Young's modulus with any increase in load conditions.

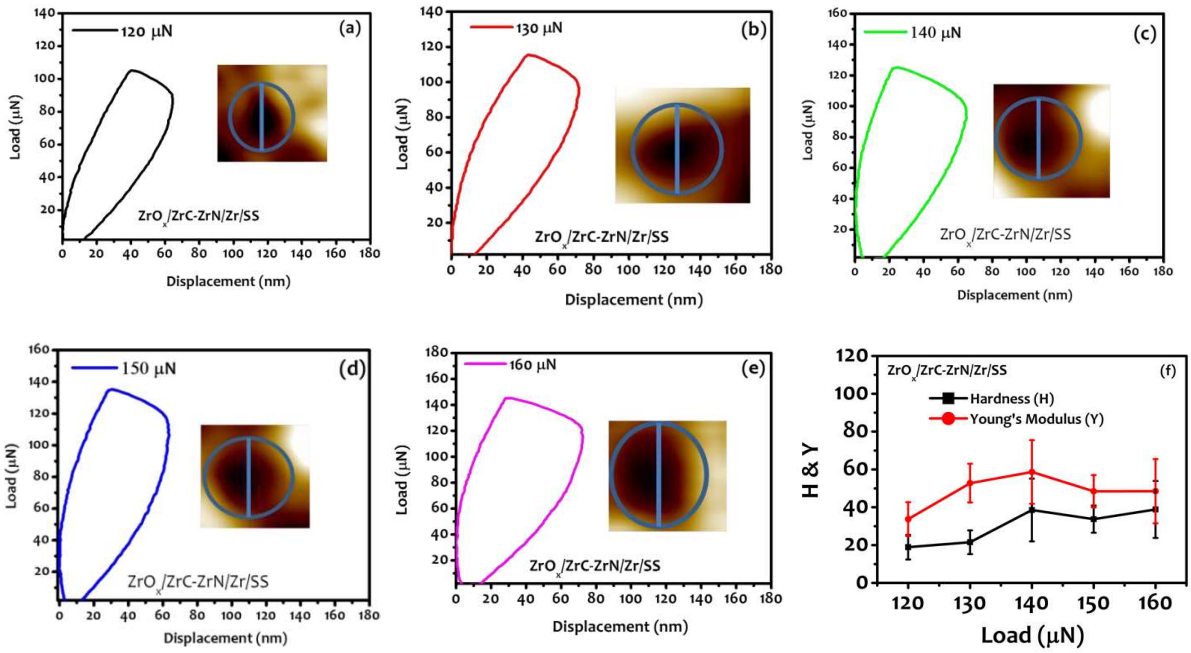


**Figure 5.14 :** The load versus displacement curve at difference end loads (a-e) with inset showing the respective AFM indentation profiles and Hardness and Young's modulus values versus load (f) for $ZrO_x$/ZrC-ZrN/Zr tandem structure with ZrC-ZrN absorber layer synthesized at 12 SCCM nitrogen flow.

## 5.6 THERMAL STABILITY IN AIR AND VACUUM OF $ZrO_X$/ZrC-ZrN/Zr ABSORBER-REFLECTOR TANDEM STRUCTURES

The thermal stability of these solar selective coatings is important especially for high-temperature applications maintaining high spectral selectivity. The STA measurements are shown in Figure 5.12(a & b) (right panel) suggesting that SSCs are thermally stable up to 700°C or higher in an inert atmosphere, as no peak has been observed in derivative of weight change (WC). In contrast to the inert ambient, these structures start degrading in air at much lower temperatures ~ 200°C, Figure 5.12(b) (Right panel). This is mainly due to the oxidation of layered tandem structures, which is more plausible in the air, suggesting that the structure can be used for high-temperature application in a vacuum or inert environment whereas at moderate temperature (< 200°C) in air/open environmental conditions.

The sample S5 with optimized selectivity has been annealed at 700$^0$C and 600$^0$C in vacuum for one and half hours for SS and Cu substrates, respectively and at 200$^0$C for one hour in the air for both the substrates to understand the structure-property correlation and its impact on solar thermal performance. The details about the structural degradation and related vibrational properties of the annealed tandem absorber-reflector structure are explained by Usmani et al. [Usmani *et al.*, 2016b]. The microstructural measurements of heat treated S5 coating surfaces on both SS and Cu substrates are shown in Figure 5.15(a) and 5.15(b), respectively. It can be seen that the degradation is clearly visible in these heat treated sample with respect to as-deposited sample, as shown in Figure 5.15. The vacuum annealed sample are less affected as compared to air-annealed samples. Moreover, the selective structure on stainless substrates is less affected with respect to that on copper substrates as shown in Figure 5.15. The large microcracks, in the case of air, annealed selective surface on copper substrates is because of the large thermal mismatch between the zirconium based layered structures, especially $ZrO_x$ phase, and copper substrates. However, SS substrates show less thermal mismatch with zirconium layered structure, especially $ZrO_x$ phase, as shown in Figure 5.15(a). In air ambient,

large surface defects were generated due to the development of $ZrO_x$ phase by transferring nitride and carbide phases in zirconium oxide phase. 3D AFM images of annealed S5 samples are shown in Figure 5.16, including vacuum and air annealed structures on SS and Cu substrates. The roughness were increased by ~ 15% for the selective structures on SS substrates for both vacuum and air annealed samples, whereas this became worse in case of selective structures on Cu substrates and the roughness values have shown increase up to ~ 47% and 82% with respect to as-prepared structures for 600°C vacuum and 200°C air annealed samples. The microstructural and surface changes, especially in air annealed case, may affect the optical response of the deposited tandem selective structures.

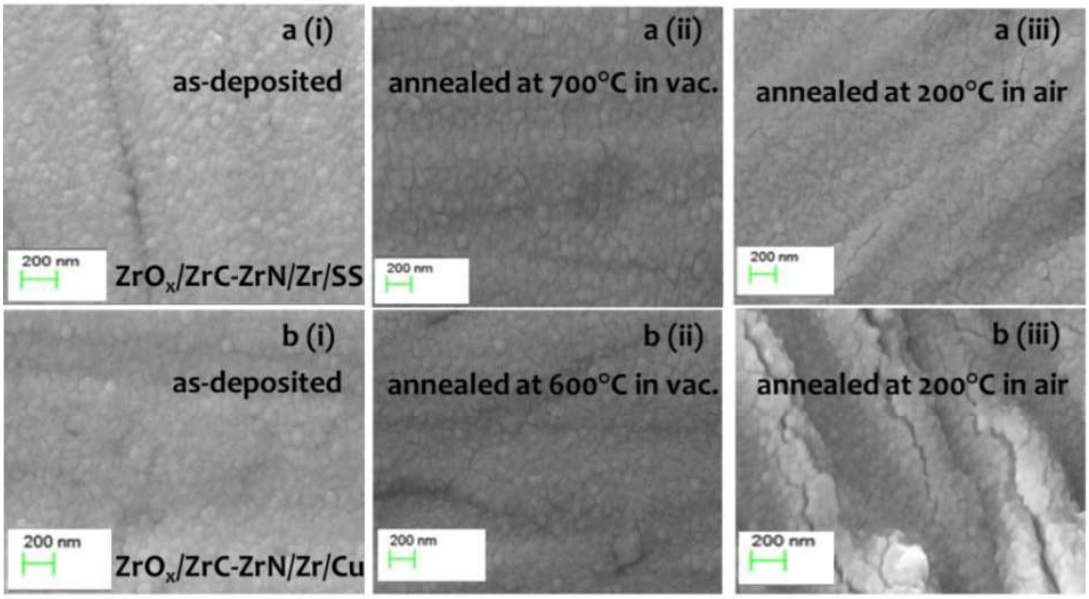


**Figure 5.15 :** SEM micrographs of heat treated $ZrO_x$/ZrC-ZrN/Zr absorber-reflector tandem structure for S5 sample on SS and Cu substrates: a(i) and b(i) as deposited; a(ii) and b(ii) annealed at 700°C/600°C in vacuum and a(iii) and b(iii) annealed at 200°C in the air on SS and Cu substrates respectively.

The reflectance spectra of these annealed tandem selective structures are shown in Figure 5.17(a) and 5.17(b) in 0.3 – 25 μm wavelength range, for S5 sample on SS and Cu substrates respectively. This measured reflectance is used to calculate the absorptance and emittance in the desired wavelength range, and results are summarized in Figure 5.17(c) and 5.17(d), suggesting that the degradation is less significant for these structure on SS substrates as compared to that on Cu substrates, where the absorptance has lowered ~ 23% after heat treatment. This is consistent with observed microstructural degradation in case of a tandem selective layer on Cu substrates.

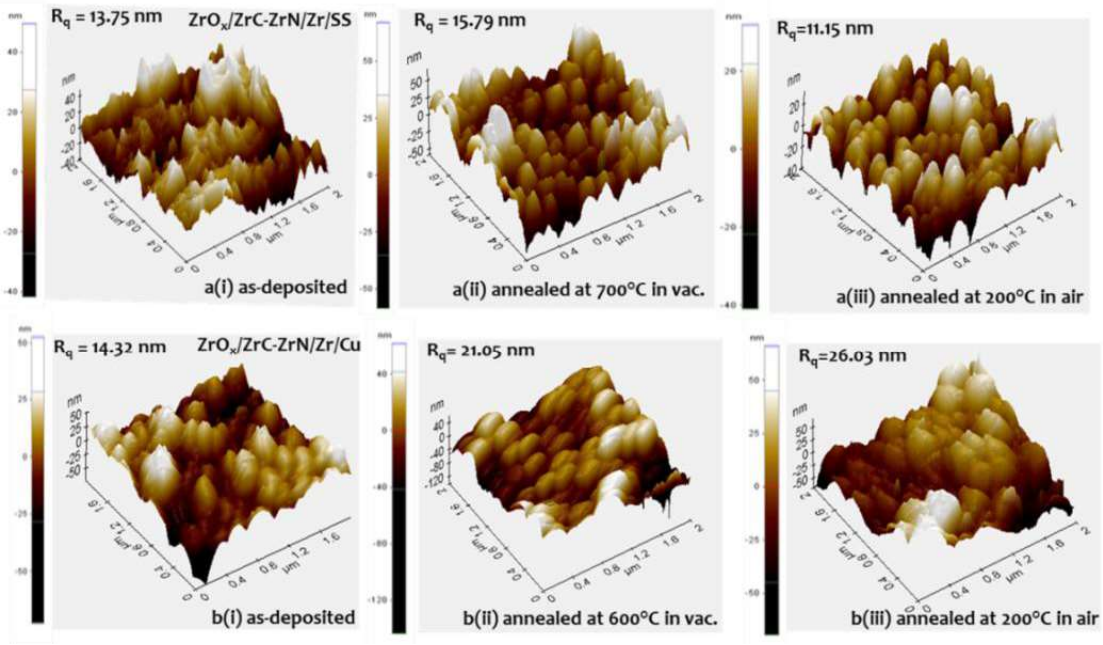


**Figure 5.16 :** Three-dimensional AFM micrographs of $ZrO_x$/ZrC-ZrN/Zr absorber-reflector tandem structure for S5 sample on SS and Cu substrate: a(i) and b(i) as deposited; a(ii) and b(ii) annealed at 700°C/600°C in vacuum and a(iii) and b(iii) annealed at 200°C in the air on SS and Cu substrates respectively.

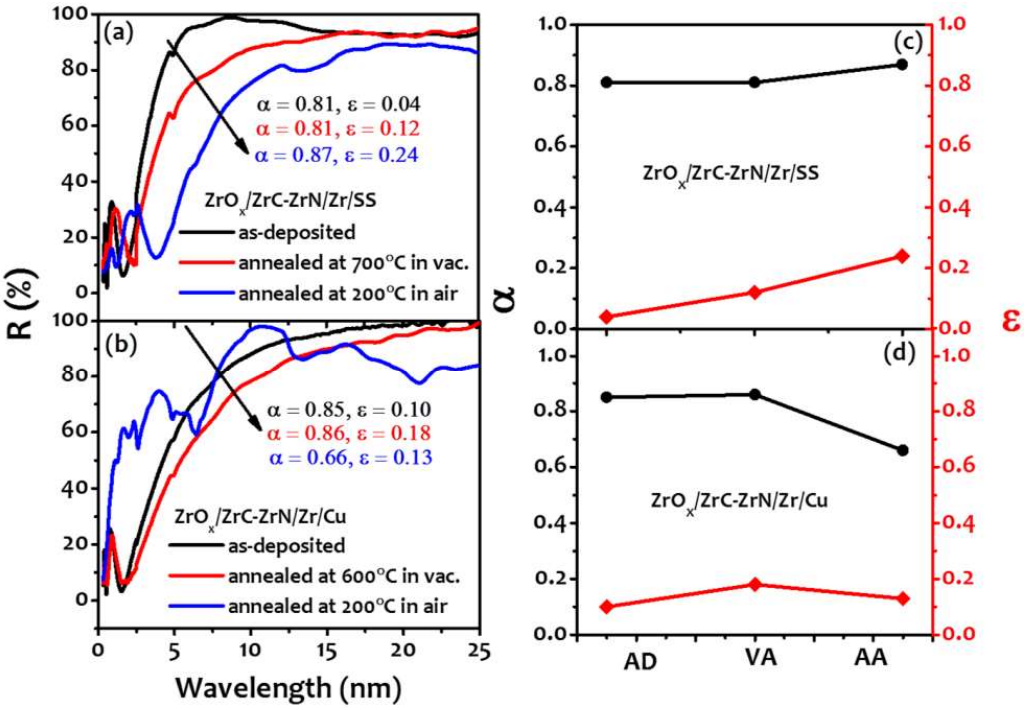


**Figure 5.17 :** % Reflectance versus wavelength for $ZrO_x$/ZrC-ZrN/Zr absorber-reflector tandem structures: a and b as-deposited, heat-treated at 700°C/600°C in vacuum for 1.5 hours and at 200°C in air for 1 hour for S5 sample on SS and Cu substrate respectively; and c and d absorptance (α) and emittance (ε) for as-deposited and heat treated S5 sample on SS and Cu substrate, where acronyms AD, VA, and AA represent as-deposited, vacuum annealed and air annealed samples.

## 5.7 CORROSION STUDIES ON MICROSTRUCTURE AND MECHANICAL PROPERTIES OF $ZrO_X$/ZrC-ZrN/Zr ABSORBER-REFLECTOR TANDEM STRUCTURES

In this section, the details of corrosion studies are discussed on absorber-reflector tandem selective structures and their correlation with solar thermal performance. Corrosion degradations are investigated in 3.5wt.% NaCl (saline) solutions. The impact of these intended corrosion experiments has been investigated to understand the degradation process for pristine, vacuum and air annealed solar selective structures. The corrosion studies are investigated on $ZrO_x$/ZrC-ZrN/Zr structures deposited on both SS and Cu substrates, using electrochemical potential current density measurements. The details about the experimental process and related characterizations are explained by Usmani et al. [Usmani *et al*., 2016e].

### 5.7.1 Results and Discussion

#### *5.7.1.1 Corrosion Studies on Substrates and $ZrO_x$/ZrC-ZrN/Zr Structures in 3.5 wt.% NaCl Solution*

The potentiodynamic polarization measurements were carried out in 3.5 wt.% NaCl electrolyte solutions at different scan rates, as explained in section 3.3.10.2. Bare SS and Cu substrates, as-deposited and thermally treated $ZrO_x$/ZrC-ZrN/Zr tandem structures on SS and Cu substrates are used as working electrode in three electrode configurations. The measured voltage versus logarithmic of current results are summarized as Tafel plots in Figure 5.18 (left panel). These measurements were collected at different scan rates to understand its impact on corrosion dynamics. The estimated corrosion results are summarized in Table 5.4 (a & b) for SS substrate and tandem selective structures on SS substrate. The corrosion current ($I_{corr}$) and potential ($E_{corr}$) are taken at the intersection points of extrapolated anodic and cathodic Tafel curves of Figure 5.18. The polarization resistance is calculated using the Stern-Geary equation $R_P = \frac{b_c \times b_a}{2.3 \times i_{corr}\left(b_a + b_c\right)}\left(K\Omega.cm^2\right)$, where $b_c$ and $b_a$ are the slopes of cathodic and anodic Tafel lines, $i_{corr}$ is corrosion current density ( $\mu A/cm^2$) and $R_P$ is the polarization resistance ($K\Omega.\ cm^2$) [Stern and Geary, (1957) (37)]. These results suggest that the corrosion current increases linearly with scan rates for all the samples under investigation, as indicated in the insets in respective Figure 5.18. The corrosion current ($I_{corr}$) is lower ~ 0.555 μA for tandem selective deposited SS substrate as compared to 2.07 μA for SS substrate at a maximum scan rate of 50 $mVs^{-1}$, suggesting that corrosion resistivity has increased for coated structures as compared to that of bare substrates. The similar behavior has been observed for other scan rates and respective corrosion currents are listed in Table 5.4 for these samples. Corrosion potential ($E_{corr}$) and polarization resistance ($R_P$) values also increase with increasing scan rates. These values are lower for tandem selective structures on SS substrate with respect to that of bare substrates. The detailed measurements of respective parameters are summarized in Table 5.4 for SS substrate.

The scan rate has a strong effect on the corrosion parameters such as corrosion potential and corrosion current density. Figure 5.19a, shows the respective changes in corrosion potential ($E_{corr.}$) and corrosion current density ($i_{corr.}$), as a function of san rate. The corrosion potential of bare 304 SS is decreased from -0.1353V to -0.4148V as the scan rate increases from 1mV/s to 50mV/s (Fig. 5.19a). Moreover, corrosion current density ($i_{corr.}$) has increased from 0.0210 $\mu A/cm^2$ to 0.684 $\mu A/cm^2$ as scan rate increases from 1 mV/s to 50 mV/s (Fig.5.19b). This phenomenon occurs due to the fast attack of corrosion elements to the coating surfaces. However, at low scan rate (1mV/s), corrosion potential, -0.0655V of tandem structure deposited on stainless steel substrate has increased from corrosion potential, -0.1353V, of bare SS substrate (Fig.5.19a). In contrast, the corrosion current density $i_{corr.}$, 0.00135$\mu A/cm^2$, of tandem selective structure coated SS substrate has decreased as compared to that of the bare SS substrate, 0.0210$\mu A/cm^2$ (Fig.5.19b). These measurements suggest that the selective surface coated substrate have better corrosion resistance ~ 1379 KΩ as compared to that of the bare substrate (382 KΩ) (Table 5.4). Thus, the observed increase in corrosion resistance for the tandem selective film on SS substrate is three times higher than that of the bare SS substrates. This is because of

the top zirconium oxide ($ZrO_x$) layer, which may act as a passivation layer to the absorber surface and thus, may prevent the surface from corrosion attacks [Barshilia *et al.*, 2004; Grips *et al.*, 2006].

These observations suggest that tandem ($ZrO_x$/ZrC-ZrN/Zr) selective structures act as corrosion protecting layer in conjunction with their solar absorbing properties on SS substrate. The observed high corrosion resistance for spectrally selective $ZrO_x$/ZrC-ZrN/Zr structures is consistent with the reported literature [Liu *et al.*, 2001; Barshilia *et al.*, 2004; Shinn *et al.*, 1992; Aydoğdu and Aydinol, 2006; Huang *et al.*, 2007a; Huang *et al.*, 2007b]. Zirconium oxide ($ZrO_x$) layer in the tandem selective structure also acts as a corrosion barrier against the bare substrate, because of its chemical and electrical inertness. The observed corrosion may be explained by introducing surface reactions as explained in Figure 5.20, where different ions from electrolytic solution start reacting with the surface and start penetrating into lower layered structures. The most common $OH^-$, $Cl^-$ and $Na^+$ electrolyte ions are reacting with metallic Zr and nitrogen elements in absorber layer, and converting it into respective chlorides, nitrates etc. The corrosion is mostly initiating at surface micro cracks or corners, where layered structures are relatively prone to such degradations.

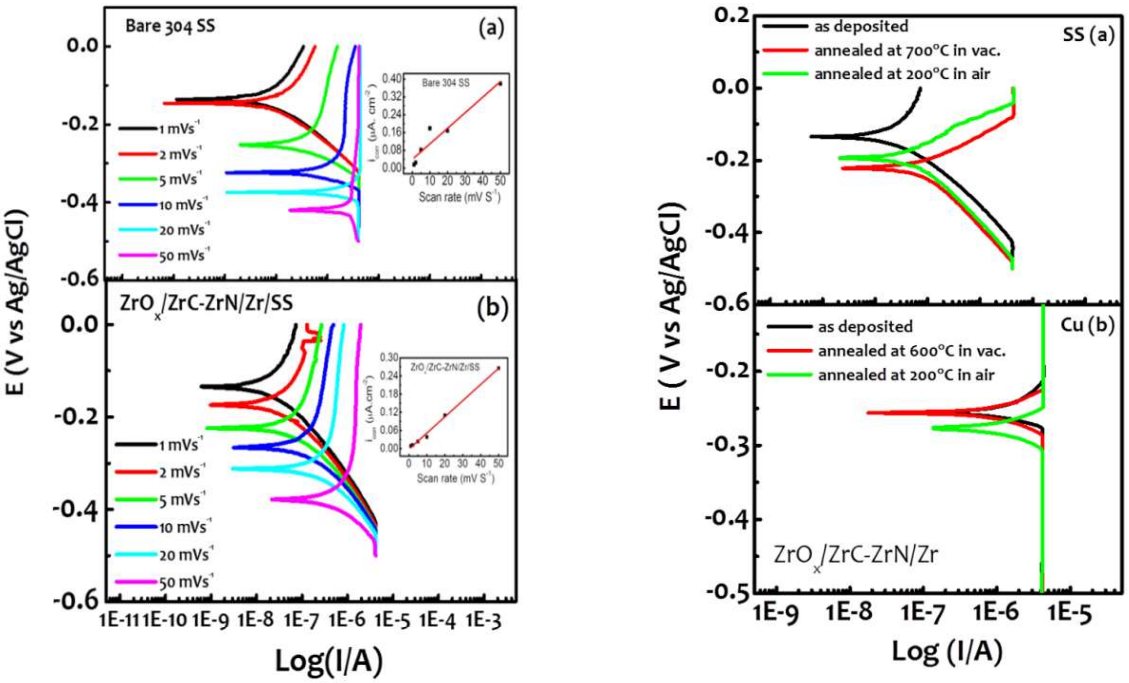


**Figure 5.18 : (Left Panel)** Potentiodynamic polarization curves for **(a)** bare 304 SS and **(b)** ARTSSCs ($ZrO_x$/ZrC-ZrN/Zr) deposited on SS substrates, in 3.5 wt.% NaCl solutions, for different scan rates. **(Right Panel)** Potentiodynamic polarization curves of as-deposited, vacuum and air annealed ARTSSCs ($ZrO_x$/ZrC-ZrN/Zr) deposited on **(a)** 304 SS and **(b)** Cu substrates in 3.5 wt.% NaCl solution at scan rate 1 $mVs^{-1}$.

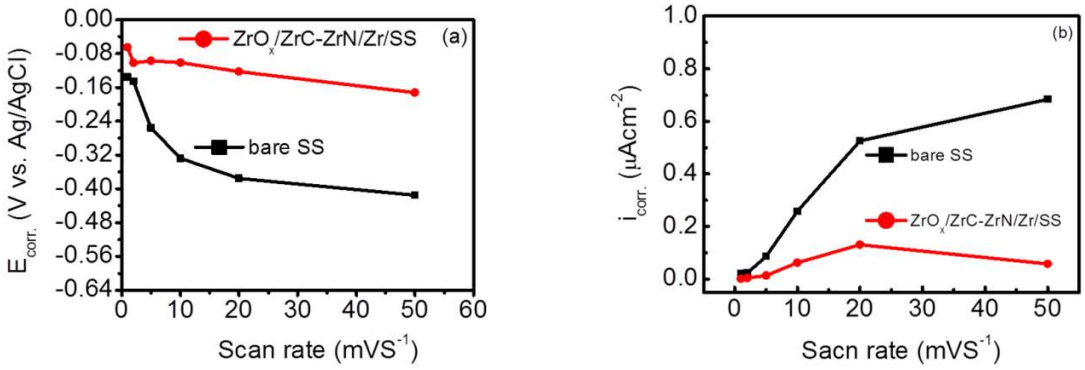


**Figure 5.19 :** Variation of **(a)** Corrosion potential ($E_{corr.}$) and **(b)** Corrosion current density ($i_{corr.}$) of bare SS and $ZrO_x$/ZrC-ZrN/Zr absorber-reflector tandem structure coated on SS substrate with varying scan rate.

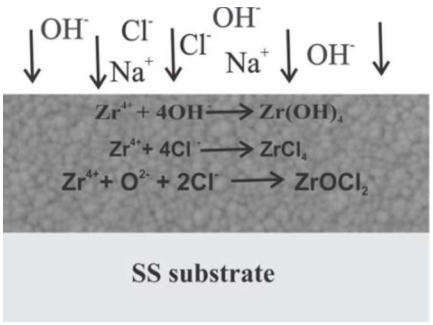


**Figure 5. 20 :** A schematic illustration of electrochemical corrosion attack of $ZrO_x$/ZrC-ZrN/Zr ARTSSCs on SS substrate in 3.5 wt.% NaCl solution.

The potentiodynamic polarization curves of annealed tandem selective structure on SS and Cu substrates are shown in Figure 5.18 (right panel), at 1 mVs$^{-1}$ scan rate in 3.5 wt.% NaCl electrolyte solution. The estimated corrosion parameters from potentiodynamic polarization measurements are summarized in Table 5.5(a) and 5.5(b) for as-deposited (AD), vacuum annealed (VA) and air annealed (AA), tandem selective structures on SS and Cu substrates, respectively. These measurements suggest that the vacuum annealed tandem selective structures on both SS and Cu substrate degrade significantly as the corrosion rates are nearly an order of magnitude higher as compared to the as-deposited structures. This is because of the induced oxygen vacancies during vacuum annealing, which make the surface prone to react at oxygen vacancy active sites in a corrosive environment, causing enhancement in the corrosion rates. However, air annealed tandem selective structures exhibit reduced corrosion rates, very similar to the pristine as-deposited structures. The air annealing of tandem selective structures does not create oxygen vacancies in the surfaces, leaving the surface intact or even enhanced oxygen stoichiometry unlike in the case of vacuum annealed case. The stoichiometric $ZrO_x$ top surface may assist in protecting structures from corrosion attacks, as confirmed by these experimental findings.

**Table 5.4 :** The estimated corrosion parameter of (a) bare 304 SS substrate and (b) $ZrO_x$/ZrC-ZrN/Zr ARTSSCs deposited on SS substrate derived from Tafel analysis of polarization curves.

| (a) Tafel data for 304 SS | | | | | | |
|---|---|---|---|---|---|---|
| **Scan rate** | **1 $mVs^{-1}$** | **2 $mVs^{-1}$** | **5 $mVs^{-1}$** | **10 $mVs^{-1}$** | **20 $mVs^{-1}$** | **50 $mVs^{-1}$** |
| $E_{corr}$ (V) | -0.1353 | -0.1462 | -0.256 | -0.3276 | -0.3752 | -0.4148 |
| $I_{corr}$ (μA) | 0.0635 | 0.07726 | 0.262 | 0.782 | 1.59 | 2.07 |
| $i_{corr}$ ($\mu A.cm^{-2}$) | 0.0210 | 0.0240 | 0.0866 | 0.258 | 0.526 | 0.684 |
| $R_p$ (K Ω) | 382 | 286 | 72.1 | 23.1 | 10.6 | 18.7 |
| $b_a$ (V/dec) | 0.159 | 0.107 | 0.163 | 0.164 | 0.103 | 0.181 |
| $b_c$ (V/dec) | 0.086 | 0.087 | 0.059 | 0.056 | 0.063 | 0.175 |
| C. Rate (mm/y) | 0.000216 | 0.000247 | 0.000891 | 0.002655 | 0.005411 | 0.007032 |
| **(b) Tafel data for $ZrO_x$/ZrC-ZrN/Zr/SS** | | | | | | |
| $E_{corr}$ (V) | -0.06555 | -0.1025 | -0.0973 | -0.1018 | -0.123 | -0.1726 |
| $I_{corr}$ (μA) | 0.02075 | 0.01923 | 0.0958 | 0.3116 | 0.637 | 0.555 |
| $i_{corr}$ ($\mu A.cm^{-2}$) | 0.00135 | 0.0042 | 0.014 | 0.0628 | 0.131 | 0.058 |
| $R_p$ (K Ω) | 1379 | 769 | 470.95 | 257.45 | 134.7 | 46.65 |
| $b_a$ (V/dec) | 0.098 | 0.11 | 0.122 | 0.153 | 0.146 | 0.195 |
| $b_c$ (V/dec) | 0.067 | 0.065 | 0.062 | 0.073 | 0.078 | 0.091 |
| C. Rate (mm/y) | 0.000054 | 0.000164 | 0.0000745 | 0.000154 | 0.000364 | 0.00358 |

In addition, the polarization measurements (for 1mV/s scan rate) have been used for calculating the protective efficiency, $P_i$ (%), for as deposited (AD), vacuum (VA) and air annealed (AA) samples using equation $P_i(\%) = \left[1 - \left(\frac{i_{corr}}{i^0_{corr}}\right)\right] \times 100$, where $i_{corr}$ and $i^0_{corr}$ represents the corrosion current density of tandem structure and substrate, respectively [Yoo *et al.*, 2008]. The AD selective structure on SS substrate showed the highest protective efficiency of 93.58% caused by lowest corrosion current density of 0.00135μA/$cm^{-2}$, as compared to the VA and AA structures (Table 5.5). The porosity of these structures was calculated from corrosion potential ($E_{corr}$) and polarization resistance ($R_p$) measurements (for 1mV/s scan rate), inferred from the potentiodynamic polarization technique, using equation $p = \left(\frac{R_{ps}}{R_p}\right) \times 10^{-\frac{\Delta E_{corr}}{b_a}}$, where $P$ is the total coating porosity, $R_{ps}$ is the polarization resistance of the uncoated substrates, $R_p$ is the polarization resistance of the coated substrate, $\Delta E_{corr}$ the difference between the corrosion potential of the coated and uncoated substrate, $b_a$ is the anodic Tafel slope of the substrate [Alanyani and Souto, 2003]. The porosity of the as-deposited tandem selective structure coated

on SS substrate is 9.93%, a lower value as compared to that of the air annealed (7.40 X $10^1$ %), suggesting that the AD tandem selective structure had a low porosity as compared to annealed one.

**Table 5.5 :** The calculated values of corrosion parameters for as-deposited, vacuum and air annealed $ZrO_x$/ZrC-ZrN/Zr ARTSSCs deposited on (a) 304 SS (b) Cu substrates, using potentiodynamic polarization measurements.

| **(a)** | **Tafel data for $ZrO_x$/ZrC-ZrN/Zr/SS at 1 $mVs^{-1}$** | | |
|---|---|---|---|
| | **As-deposited (AD)** | **Vacuum Annealed (VA) (700°C)** | **Air annealed (AA) (200°C)** |
| $E_{corr}$ (V) | -0.06555 | -0.14475 | -0.12355 |
| $I_{corr}$ (μA) | 0.02075 | 0.03445 | 0.0027 |
| $i_{corr}$ (μA.$cm^{-2}$) | 0.00135 | 0.8605 | 0.0245 |
| $R_p$ (K Ω) | 1379 | 104 | 435 |
| $b_a$ (V/dec) | 0.098 | 0.066 | 0.063 |
| $b_c$ (V/dec) | 0.067 | 0.143 | 0.068 |
| C. Rate (mm/y) | 0.000054 | 0.00144 | 0.000512 |
| **(b)** | **Tafel data for $ZrO_x$/ZrC-ZrN/Zr/Cu at 1 $mVs^{-1}$** | | |
| | **As-deposited (AD)** | **Vacuum Annealed (VA) (600°C)** | **Air annealed (AA) (200°C)** |
| $E_{corr}$ (V) | -0.1535 | -0.1531 | -0.1733 |
| $I_{corr}$ (μA) | 0.303 | 0.192 | 0.253 |
| $i_{corr}$ (μA.$cm^{-2}$) | 0.722 | 0.574 | 0.386 |
| $R_p$ (K Ω) | 7.223 | 9.974 | 8.548 |
| $b_a$ (V/dec) | 0.048 | 0.038 | 0.032 |
| $b_c$ (V/dec) | 0.022 | 0.03 | 0.028 |
| C. Rate (mm/y) | 0.01402 | 0.01138 | 0.00805 |

#### *5.7.1.2 Structure-Property Correlation for Corrosion Treated $ZrO_x$/ZrC-ZrN/Zr Structures*

The structural and microstructural properties for these corrosion treated tandem spectrally selective surfaces are explained by Usmani et al. [Usmani *et al.*, 2016e]. The corrosion resistance of these tandem selective structures also depends on packing density of microstructure/granular geometries and in general, the corrosion current density, $i_{corr}$, decreases with increasing the packing density. Corrosion treated air annealed tandem selective structures showed corrosion current density ~ 0.0245 μA/cm$^2$, which is less than that of vacuum heat treated tandem selective structure ~ 0.8605 μA/cm$^2$, but higher than as deposited tandem selective structure ~ 0.00135 μA/cm$^2$. Air annealed selective structure showed high corrosion resistance, suggesting enhanced stoichiometric $ZrO_x$ formation as compared to that of heat treated tandem selective structures under vacuum, which is oxygen deficient [Huang *et al.*, 2007; Kubaschewski, 1993]. The oxygen deficient $ZrO_x$ is a relatively good electrical conductor and oxygen vacancies provide corrosion attacking sites and thus showing enhanced corrosion current density, consistent with experimental observations. Also, electrical conductivity is a good measure of the corrosion current density (CCD) and higher electrical resistance may result in lower CCD, $i_{corr}$ at the same applied potential and thus may exhibit higher corrosion resistance [Huang *et al.*, 2008]. The similar microstructural degradation and corrosion behavior have been observed for corrosion treated tandem selective structures on Cu substrates.

#### *5.7.1.3 Mechanical Degradation of Corrosion Treated $ZrO_x$/ZrC-ZrN/Zr Structures*

The measured load versus displacement curves are shown in the Figure 5.21 (left panel) for AD, VA and AA tandem selective structure after corrosion treatment. The initial force was set at 14.3 μN for all nanoindentation measurements and also measurements are corrected for any residual backgrounds. The nanoindented area A was estimated by averaging ten such indentations for calculating Young's modulus (YM) and hardness values for these structures, following Oliver and Pharr methodology for analyzing the measurements [Oliver and Pharr, 2004, 1992a].

The estimated YM and hardness values are shown in Figure 5.21 (right top panel) suggesting that both reduced drastically for corrosion treated air annealed tandem selective structures. Also, both values reduced to ~ 50% of the untreated as deposited and vacuum annealed samples. This is because of relatively large microstructural degradation, due to the oxygen diffusion inside multilayer structures for air annealed samples. The observed reduction in both hardness and Young's modulus values for corrosion treated air annealed (AC-AA) tandem structure (from 17.85 GPa to 7.60 GPa and 60.48 GPa to 30.10 GPa) as compared to AD structures, substantiate the observed relatively large microstructural degradation such as increased grain size and enhancement in the oxygen content in corrosion treated air annealed samples. The small amount of oxygen can modify the film properties, and oxygen segregation at the grain boundaries can also contribute to interface embrittlement [Riedl *et al.*, 2016]. This may lead to a change in fracture mode from intra- to inter-granular [De Hosson and Cavaleiro, 2006]. Moreover, increasing the content of oxygen in coating also acts as a softening factor in the coatings [Vaz *et al.*, 2004]. Hall-Petch relationship suggests that the materials' mechanical strength can be increased by reducing the grain size in a material [Sylwestrowicz and Hall, 1951; Petch, 1953]. Thus, a small grain size could be beneficial for mechanical strength. In addition, the oxygen impurities at grain boundaries in coatings may lead to the embrittlement because of the wrecking of the grain boundaries [Veprek, and Veprek-Heijman, 2012]. Thus, the observed relatively poor YM and hardness are because of microstructural defects such as enhancement in grain size and oxygen content in the coatings, introduced during corrosion. The observed degradation has a severe impact on solar thermal properties of these structures.

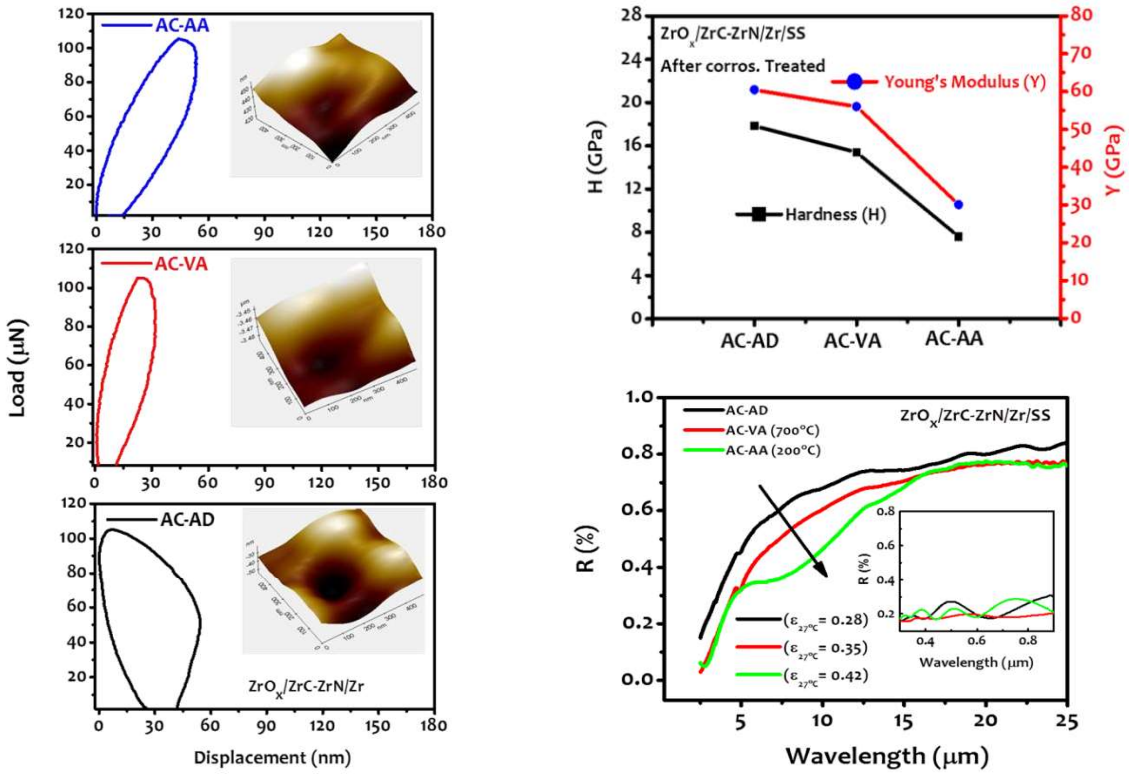


**Figure 5.21 :** The load (P) versus displacement curves of corrosion treated AD, AV and AA ARTSSCs coated on SS substrate at load 120 μN, with inset showing representative AFM nanoindentation areal profile **(Left panel);** Hardness (H) and Young's modulus (Y) of corrosion treated AD, AV and AA ARTSSCs coated on SS substrate at 120 μN **(Top right panel);** Reflectance spectra of corrosion treated as-deposited (AC-AD), vacuum (AC-VA) and air (AC-AA) annealed ARTSSCs coated on SS substrates, in 3.5 wt.% NaCl solution **(Bottom right panel).**

### *5.7.1.4 Optical Degradation of Corrosion Treated ZrO$_x$/ZrC-ZrN/Zr Structures*

The tandem selective structures (ZrO$_x$/ZrC-ZrN/Zr/SS) exhibit optical degradation after corrosion treatments. The observed degradations are consistent with the proposed corrosion attack pathways, as illustrated in Figure 5.20. To understand the impact on solar thermal performance, reflectance spectra were collected in the range of 0.3 – 0.9 μm (UV-Vis range) and 2.5 – 25 μm infrared range on these corrosion treated tandem selective structures. The results are plotted in Figure 5.21 (bottom right panel). The calculated absorptance and emittance values suggest that the absorptance of corrosion treated tandem selective structure remain unaffected, however, emittance values increased drastically to 0.28, 0.35 and 0.42 for AD, VA, and AA tandem selective (ZrO$_x$/ZrC-ZrN/Zr/SS) structures. The observed increase in emittance is consistent with the observed structural and microstructural degradation, as emittance is a surface sensitive property. The corrosion has a severe impact on the microstructural degradation of surface structures for all investigated samples, which is directly related to the emittance values. The similar degradation on solar thermal properties has been observed for such spectrally selective structures on Cu substrates.

## 5.8 SOLAR PERFORMANCE ANALYSIS OF $ZrO_x$/ZrC-ZrN/Zr ABSORBER-REFLECTOR TANDEM STRUCTURES UNDER EXTREME THERMAL ENVIRONMENT

In this section, the effect of thermal degradation at elevated temperatures up to 900°C, in both nitrogen and air environments, has been discussed for $ZrO_x$/ZrC-ZrN/Zr/SS structures. We carried out intensive structure – properties measurements after such extreme thermal treatments to understand the materials' degradation and related solar thermal performance.

### 5.8.1 Results and Discussion

#### *5.8.1.1 Structural, Microstructural, Morphology and Elemental Analysis*

X-ray diffraction analysis on thermally treated $ZrO_x$/ZrC-ZrN/Zr/SS structures at elevated temperature (up to 900°C) exhibited only tetragonal, monoclinic and cubic phases of $ZrO_x$ material. The SEM micrographs are shown in Figure 5.22 for both nitrogen and air annealed $ZrO_x$/ZrC-ZrN/Zr/SS structures. The surface defects such as micro-cracks are clearly visible, as marked by arrows for clarity, in Figure 5.22, which are not seen in the case of AD samples, as discussed in previous sections. The AFM measured surface roughness are much larger ~ 26.21 nm and ~ 22.67 nm for heat treated samples under nitrogen and air environments respectively, as compared to that of ~ 13.75 nm for as untreated ARTSSC's samples [Usmani *et al.*, 2016f].

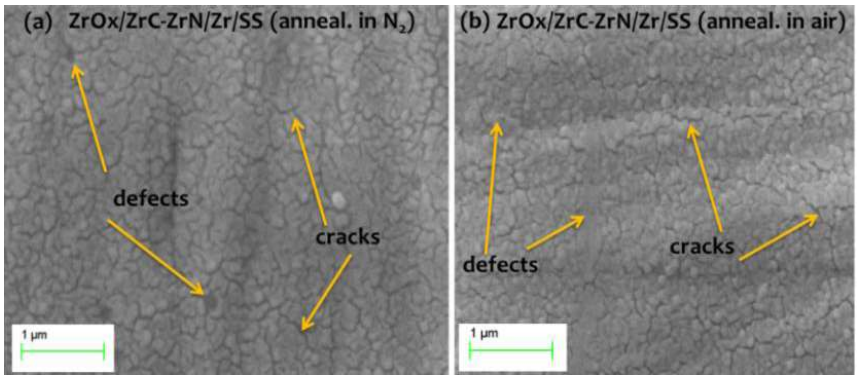


**Figure 5.22 :** SEM images of heat treated $ZrO_x$/ZrC-ZrN/Zr/SS ARTSSCs in (a) $N_2$ and (b) air environments up to 900°C.

The observed degradation, in carbide and nitride phases of the absorber layer and their possible conversion into different zirconium oxide phase, as observed from XRD measurements, was also substantiated by EDX measurements on heat treated $ZrO_x$/ZrC-ZrN/Zr/SS ARTSSC's structures [Usmani *et al.*, 2016f]. A systematic increase in oxygen atomic fraction and decrease in nitrogen and carbon atomic fractions have been observed and results substantiate the observed oxide phases only, as explained earlier. Increased atomic fraction of oxygen in these heat treated ARTSSC's structures, possibly has increased defects and surface roughness as compared to the as-deposited structures. The absence of nitrogen content in these structures may be due to the EDX measurement limitations of the instrument and thus, unable to notice the presence of any small nitrogen fraction in these samples, like the observed XRD measurements. The defect density and surface roughness values are much larger in the case of heat-treated samples under air ambient, with the respect that of samples treated under nitrogen environment. This is because of the enhanced oxygen atomic fraction, causing severe changes from carbide/nitride phases into $ZrO_x$ phases, leading to the larger structural and surface damages in case of air treated samples.

#### *5.8.1.2 Mechanical and Optical Properties Analysis*

The representative force - displacement curves, for 120 μN force, are plotted in Figure 5.5.23(a) with a respective AFM indentation profile, Figure 5.23(b), on annealed tandem selective structure on SS substrate under air environment. Numerous such force-displacement curves were carried out for different force conditions and used to extract the variation of the hardness and Young's modulus as a function of applied force. The results are plotted in Figure 5.23(c) and 5.23(d) for annealed tandem selective structures under nitrogen and air environments, respectively. The hardness values decreased initially with force and saturated to ~ 7.07 GPa and ~ 5.42 GPa values for annealed samples in nitrogen and air ambient. These values are much smaller than that of ~ 18.88 GPa for AD tandem selective structure samples. This is consistent with our proposed hypothesis of ZrN-ZrC loss during heat treatments and also supported by XRD and EDX measurements. The similar behavior has been observed on other spectrally selective structures [Huang *et al.*, 2007, Huang *et al.*, 2011a, 2011b, 2009c; Fang and Chang, 2004]. The nitride and carbide phases are converted into oxides by oxidation of ZrC-ZrN during heat treatment and thus, resulted into reduced hardness for these structures. The ZrN phase is much harder than $ZrO_x$ and thus the loss of ZrN from the absorber structure may be attributed to the observed poor hardness values. In addition to these changes, the respective structural/microstructural degradation, such as cracks, larger gains etc., of these heat treated samples is also responsible for the observed poor hardness values. In contrast to hardness, Young's modulus of these heat treated samples did not exhibit strong variation, as shown in Figure 5.23(d), yet the measured values of Young's modulus for annealed sample in the air are always lower as compared to that of heat treated in a nitrogen environment. This may be due to the relatively large microstructural defects in air treated ARTSSCs with respect to that of nitrogen treated ARTSSCs.

The observed structural/microstructural, and surface changes (i.e. degradations) have an impact on optical response, for these structures. The measured reflectance spectra for heat treated ARTSSC's structures are plotted in Figure 5.24 for both environmental conditions. We observed that the reflectance of heat treated ARTSSC's in the air is always lower as compared to that of in nitrogen treated sample. This is again consistent with the observations of relatively larger defects in air treated samples. The measured absorptance values are ~ 0.70 and ~ 0.68 for heat treated ARTSSC's in nitrogen and air, respectively. These values are relatively smaller than that of as-deposited ARTSSC's (~ 0.88). The measured emissivity values are 0.25 and 0.28 for heat treated ARTSSC's in nitrogen and air, respectively and are much higher than that of as-deposited ARTSSC's structure ~ 0.04. The observed lower absorptance and higher emittance can be attributed to the enhanced structural and microstructural defects, developed during thermal treatment of these ARTSSC's structures under such extreme (~ 900°C) conditions.

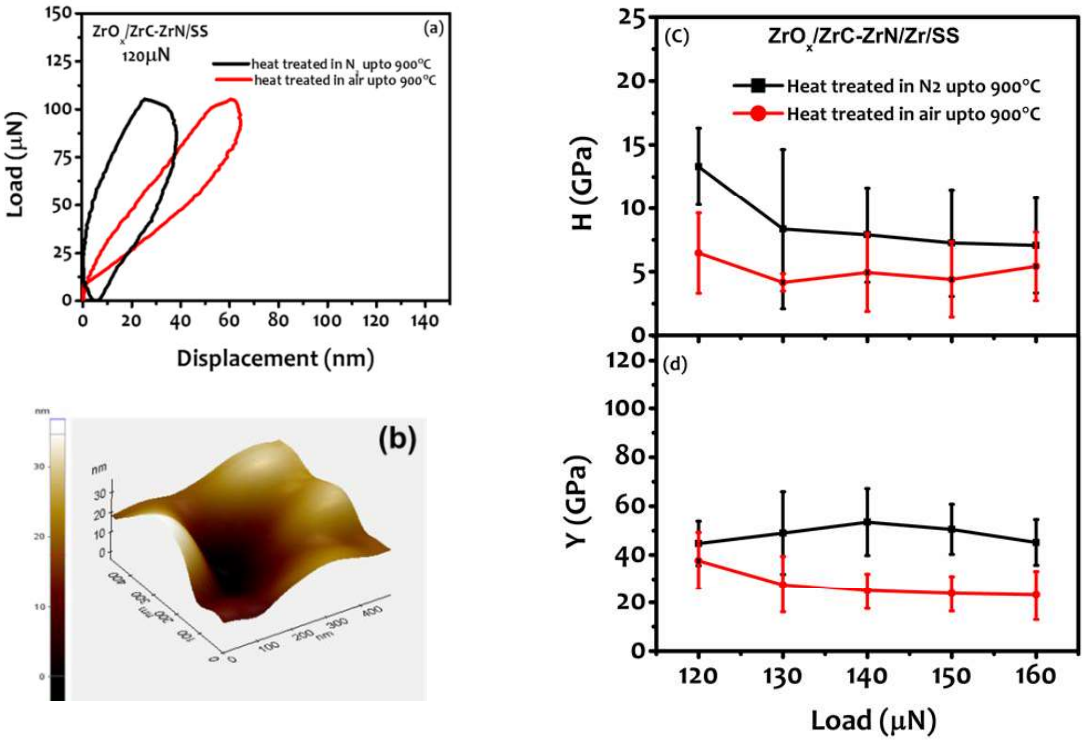


**Figure 5.23 : (a)** Force Vs displacement curve at 120μN for heat treated $ZrO_x$/ZrC-ZrN/Zr/SS ARTSSCs in $N_2$ and air environments up to 900°C, **(b)** AFM indentation profile of an indentation, **(c)** Hardness **(H)** and **(d)** Young's Modulus (Y) versus applied force for heat treated $ZrO_x$/ZrC-ZrN/Zr/SS ARTSSCs in $N_2$ and air environment.

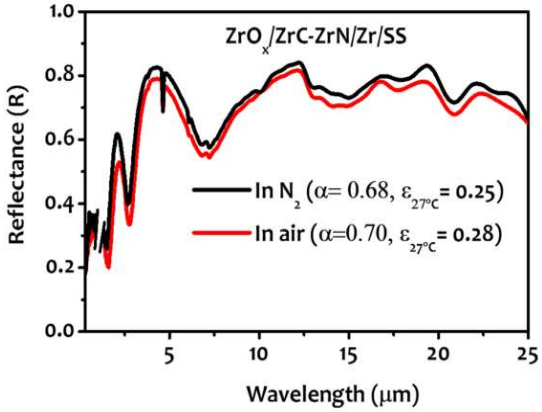


**Figure 5.24 :** Reflectance spectra of heat treated $ZrO_x$/ZrC-ZrN/Zr/SS ARTSSCs structures in $N_2$ and air environment up to 900°C.

## 5.9 CONCLUDING REMARKS

DC magnetron sputtered zirconium (Zr) films have been optimized in order to achieve the minimum thermal emittance in 2.5 – 25 μm wavelength range on different substrates. Optimized sputtered parameters for zirconium films such as deposition time ~ 120 min – 150 min and deposition temperature as ~ 300°C – 350°C, showed the minimum thermal emittance values 0.12 and 0.14 on SS and glass substrate. These optimized conditions are used for Zr deposition in ZrOx/ZrC-ZrN/Zr structure development. Further, ZrOx/ZrC-ZrN/Zr absorber-reflector tandem structures were successfully deposited on SS, Cu, Al and glass substrates. The growth conditions are optimized by varying nitrogen flow rate during the ZrC-ZrN absorber deposition for the maximum absorptance. The presence of nitrogen during deposition has shown strong dependence on optical performance, with ~ 12.5 SCCM nitrogen flow rate, the ZrC-ZrN absorber layer exhibited the best solar performance (selectivity) such as absorptance ~ 0.81, 0.85, 0.86 & 0.86 and emittance ~ 0.04, 0.1, 0.05 & 0.05 on SS, Cu, Al and glass substrates. Further, mechanical properties such as Young's modulus and hardness increases from ~ 19.63 GPa to ~ 38.53 GPa and ~ 36.39 GPa to ~ 58.67 GPa with increasing nitrogen flow rate. The absorber growth conditions have a strong influence on mechanical properties and moderate hardness and Young's Modulus values may be important for the optimal solar thermal performance. Thermal stability test on $ZrO_x$/ZrC-ZrN/Zr tandem structure suggests that these tandem structures are thermally stable at ~ 600°C in a vacuum, whereas at or below 200°C in the air. The impact of corrosion on $ZrO_x$/ZrC-ZrN/Zr structure has been investigated in 3.5 wt.% NaCl saline solution. The corrosion resistance, ~ 1379 kΩ, is much larger, as compared to that of bare stainless steel, copper and aluminum substrates, suggesting high reliability for these structures in the adverse environmental conditions.

…